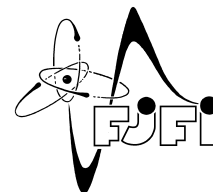




ČESKÉ VYSOKÉ UČENÍ TECHNICKÉ V PRAZE
Fakulta jaderná a fyzikálně inženýrská



Klasické a kvantové logické operace nad superpozicemi OAM

Classical and quantum logic operations on OAM superpositions

Diplomová práce

Autor: **Bc. Matyáš Staněk**
Vedoucí práce: **Ing. Václav Potoček, Ph.D.**
Akademický rok: 2020/2021

- Zadání práce -

- Zadání práce (zadní strana) -

Acknowledgement:

I would like to thank my supervisor Ing. Václav Potoček, Ph.D. for his guidance, advice and support throughout the writing of this thesis.

Čestné prohlášení:

Prohlašuji, že jsem tuto práci vypracoval samostatně a uvedl jsem všechnu použitou literaturu.

Nemám závažný důvod proti použití tohoto školního díla ve smyslu § 60 Zákona č. 121/2000 Sb., o právu autorském, o právech souvisejících s právem autorským a o změně některých zákonů (autorský zákon).

V Praze dne 21.5.2021

Bc. Matyáš Staněk

Název práce:

Klasické a kvantové logické operace nad superpozicemi OAM

Autor: Bc. Matyáš Staněk

Obor: Matematické inženýrství

Zaměření: Matematická fyzika

Druh práce: Diplomová práce

Vedoucí práce: Ing. Václav Potoček, Ph.D., Katedra fyziky, Fakulta jaderná a fyzikálně inženýrská ČVUT v Praze

Abstrakt: Světlo má mnoho stupňů volnosti a jedním z nich je orbitální moment hybnosti (OAM). Svazky nesoucí OAM se běžně popisují v ortonormální bázi Laguerre-Gaussových módů, ve které celé číslo l charakterizuje velikost OAM daného bazického stavu. V této práci využíváme neomezenosti indexu l zapsaného ve dvojkové soustavě ke kódování informace. Nejprve navrhujeme optické elementy pro aritmetické operace s hodnotou OAM a následně je využijeme k implementaci bitového posunu. Díky linearitě všech použitých prvků je možné tuto myšlenku zobecnit a na OAM pohlížet také jako na nosič kvantové informace. Pro práci jak s jedním, tak s více kvantovými bity jsou navrženy optické logické brány. V závěru studujeme proveditelnost všech navržených operací na základě numerických simulací, které odhalí jejich teoretickou účinnost.

Klíčová slova: klasické logické operace, kvantová informace, Laguerre-Gaussovy módy, orbitální moment hybnosti, prostorová fázová modulace

Title:

Classical and quantum logic operations on OAM superpositions

Author: Bc. Matyáš Staněk

Abstract: Light has many degrees of freedom and one of them is the orbital angular momentum (OAM). Beams carrying OAM are usually described in the orthonormal basis of Laguerre-Gaussian modes, in which the integer l corresponds to the value of the OAM of the given basis state. In this thesis, we take advantage of the unbounded nature of the index l to encode information in its binary representation. First we design optical elements for arithmetic operations with OAM and use them for a bit shift. Consequently, thanks to linearity of the optical components it is possible to generalize the idea and view OAM as a carrier of quantum information. We put forward an implementation of a set of optical quantum gates for single or multiple OAM qubits. Finally, theoretical efficiency of the proposed devices is studied with numerical simulations.

Key words: classical logic operations, Laguerre-Gaussian modes, orbital angular momentum, quantum information, spatial phase modulation

Contents

Introduction	7
1 Orbital angular momentum of light	8
1.1 Paraxial equation	8
1.2 LG modes	9
1.3 OAM generation	11
1.4 OAM manipulation	13
1.5 OAM detection	18
2 Classical logic operations with OAM	21
2.1 Right shift	21
2.2 Left shift	22
2.3 Example: swap of the last 2 bits	23
2.4 Operator notation of optical setups	25
3 Quantum logic operations with OAM	29
3.1 Qubits and quantum gates	29
3.2 Optical qubits on OAM superpositions	31
3.3 Optical gates for OAM qubits	33
3.4 State preparation and measurement	38
4 Realizability	39
4.1 $\times 2$ - and $/2$ -modulation with method A	39
4.2 $\times 2$ - and $/2$ -modulation with method B	44
4.3 $\pm\delta$ holograms	48
4.4 Efficiency of optical quantum gates	50
Conclusion	54
Appendix	56
A. Methods and Materials	56
B. Numerical simulations	58

Introduction

Almost 30 years ago it was recognized that a light beam with a helically shaped wavefront can carry an orbital angular momentum (OAM) [1]. Paraxial beams with OAM are usually described in the orthonormal basis of Laguerre-Gaussian modes, in which the significant part is the azimuthal phase dependence $e^{il\varphi}$. The integer l dictates how many helices forming the wavefront are intertwined together as well as the value of OAM for the given basis state. More importantly, there are no principal limitations on how large the index l can be.

Since its discovery, OAM was studied not only theoretically [2, 3], but also found a practical purpose in optical manipulation [4], communication [5] and imaging technologies, see [6] and the references therein. Additionally, this new degree of freedom of light offered innovative opportunities for experimental verification of quantum theory [7, 8, 9, 10] naturally complementing the spin angular momentum (SAM) of photons. SAM is attributed to circular polarization and can have only two values, $\pm\hbar$. The total angular momentum is then given by the sum of OAM and SAM.

Our main interest lies in the unbounded nature of the integer l , because it provides a potentially infinite dimensional state space for encoding information. By expressing the azimuthal index l in base 2, OAM can be viewed as a string of classical bits, or conversely, the optical states in different modes regarded as a basis of multiple qubits. Consequent transformations of OAM are equivalent to bitwise manipulations of the string or to quantum logical gates.

In this thesis, we first design phase modulators for performing arithmetic operations with OAM. The ability to double/halve OAM is crucial for the proposed left/right shifting operations of a bit string. Additionally, we explain the function of the parity sorters, a devices capable of sorting beams based on their OAM.

A natural generalization of classical operations is to manipulate quantum information. We treat the LG modes as computational basis states for optical qubits and design a universal set of quantum gates, for instance the elementary rotations, a few common single qubit gates and the *CNOT* gate.

The final chapter concludes the work with numerical simulations investigating the feasibility of the presented devices. The main focus of attention is on quantifying distortions and estimating the efficiency of the OAM transforming holograms.

Chapter 1

Orbital angular momentum of light

The first parts of this chapter serve as a brief review of the orbital angular momentum. At the beginning, the key assumptions are established followed by derivation of the paraxial equation. Then a specific family of solutions is presented, which illustrates the core properties of OAM. The whole picture is completed with a description of a few possible methods to generate helically phased beams as well as a list of several techniques for manipulation and detection of OAM. The optical elements presented here are mainly focused on the topic of the next chapter, representation of classical bits by beams carrying OAM and consequent bitwise manipulation.

1.1 Paraxial equation

In the classical theory of electromagnetism, light is described by Maxwell's equations. This thesis does not aspire to investigate detailed quantum effects of light-matter interactions, and therefore the classical interpretation will suffice. Moreover, to understand the main object of interest, the orbital angular momentum of light, the simplifications offered by the scalar wave theory and the paraxial approximation are sufficient.

Ignoring the vectorial nature of the electromagnetic field, a single component of a coherent monochromatic wave can be expressed as a complex function

$$u(x, y, z, t) = U(x, y, z)e^{-i\omega t}, \quad (1.1)$$

where ω is the angular frequency of the wave. OAM can be fully explained statically using the function $U(x, y, z)$ and hence the time dependency $e^{-i\omega t}$ is irrelevant and will be omitted from here on.

The paraxial approximation imposes a few restrictions on the studied field. The wave, or rather the beam, should propagate along the z axis, which validates factoring out the dominant term e^{ikz} (where $k = 2\pi/\lambda$ is the wave number) leaving only

$$U(x, y, z) = \tilde{U}(x, y, z)e^{ikz}. \quad (1.2)$$

Another requirement for the beam is to behave reasonably on a scale of a wavelength, without any extreme variations of the field distribution. The change of $\left|\frac{\partial \tilde{U}}{\partial z}\right|$ in the z direction has to be small compared to the value itself as well as the transverse variations

$$\left|\frac{\partial^2 \tilde{U}}{\partial z^2}\right| \ll \left|2k\frac{\partial \tilde{U}}{\partial z}\right| \quad \text{or} \quad \left|\frac{\partial^2 \tilde{U}}{\partial x^2}\right| \quad \text{or} \quad \left|\frac{\partial^2 \tilde{U}}{\partial y^2}\right|. \quad (1.3)$$

Under these assumptions, the main equation of the paraxial approximation can be derived from the standard Helmholtz equation for scalar monochromatic waves

$$(\Delta + k^2)U = 0 \quad (1.4)$$

in the following manner. Substituting (1.2) into (1.4) and simplifying along with (1.3) will result in [11, p. 628]

$$\frac{\partial^2 \tilde{U}}{\partial x^2} + \frac{\partial^2 \tilde{U}}{\partial y^2} + 2ik \frac{\partial \tilde{U}}{\partial z} = 0. \quad (1.5)$$

The equation (1.5) is called the paraxial equations since it governs the behaviour of all beams in this approximation.

1.2 LG modes

There are many solutions to the paraxial equation (1.5), but the most suitable one for describing OAM can be found in cylindrical coordinates. After lengthy calculations (details can be found in [12]) Laguerre-Gaussian (LG) modes

$$LG_p^l(r, \varphi, z) = \sqrt{\frac{2p!}{\pi(p+|l|)!} \frac{w_0}{w(z)}} \left(\frac{\sqrt{2}r}{w(z)}\right)^{|l|} L_p^{|l|} \left(\frac{2r^2}{w(z)^2}\right) \exp\left[\left(\frac{-1}{w(z)^2} + \frac{ik}{2R(z)}\right)r^2\right] \times \exp(il\varphi) \exp[i(1+|l|+2p)\psi(z)] \quad (1.6)$$

emerge as a set of orthogonal solutions characterized by two indices $p \in \mathbb{N}_0$, $l \in \mathbb{Z}$. The LG modes owe their name to the associated (generalized) Laguerre polynomials $L_p^{|l|}(x)$ and the Gaussian function $\exp(-r^2/w(z)^2)$ dictating the transverse intensity profile of the beam. The physical parameters of the beam, the waist w_0 and the Rayleigh range $z_R (= 1/2kw_0^2)$ [13], are encoded into the different functions in the expression (1.6), namely the spot size

$$w(z) = w_0 \sqrt{1 + \left(\frac{z}{z_R}\right)^2}, \quad (1.7)$$

the radius of curvature

$$R(z) = z + \frac{z_R^2}{z}, \quad (1.8)$$

and the Gouy phase shift

$$\psi(z) = \arctan\left(\frac{z}{z_R}\right). \quad (1.9)$$

The most important part of (1.6) is the azimuthal dependence $\exp(il\varphi)$, because it gives rise to a helical deformation of the wavefront [14]. The absolute value of the integer l dictates the number of intertwined helices, while the sign of l corresponds to the direction of rotation, as is shown in Fig.1.1. Thanks to this non-trivial (non-planar) space structure, the Poynting vector, which is always perpendicular to the phase front, has a transverse component revolving around the beam axis and hence generates an angular momentum [1]. From analogy between paraxial optics and quantum mechanics it can be deduced that LG beams containing $\exp(il\varphi)$ carry OAM equal to $l\hbar$ per photon.

Although the value of OAM originates from the expression dependant on l , the other mode index deserves a mention as well. The role of p is mainly geometrical since it controls the degree of the polynomial $L_p^{|l|}(x)$, which is then responsible for the transverse intensity profile of the beam. Figure 1.2 shows several normalized intensities of LG beams for $l \neq 0$ showing concentric rings with zero intensity on the axis [6]. During propagation through space, the spot size of the beam changes according to (1.7). (Note that $w(z)$ is not the actual width of the beam, but only a measure characterizing the behaviour of Gaussian-like beams [13].) However, apart from this radial scaling, the mode structure is stable and the intensity profile remains the same [2, p. 310].

The orthogonality of Laguerre polynomials [15, p. 282] (together with the analogy between quantum mechanics and paraxial optics mentioned earlier) suggests a new possibility how to view the LG modes. They can be thought of as eigenvectors of the quantum mechanical operator angular momentum \hat{L}_z . Moreover, such modes form a complete basis of an infinite-dimensional Hilbert space and thus it is valid to denote them with ket $|p, l\rangle$ representing a quantum photon state with the corresponding azimuthal number. In this notation, all pure LG modes have well defined value of OAM, since $\hat{L}_z |p, l\rangle = l\hbar |p, l\rangle$ [3]. Photon states of all other paraxial beams can be expressed as a superposition $|\psi\rangle = \sum_{p,l} \alpha_{p,l} |p, l\rangle$ with some complex coefficients $\alpha_{p,l}$, where the index p does not affect OAM. We will usually work with $p = 0$, in this case the value will be omitted and the state labelled as $|l\rangle$.

It is important to note that in the following text, the ket notation will not imply normalization and we will normalize the states only when needed (the basis states $|p, l\rangle$ are normalized by virtue of (1.6), though).

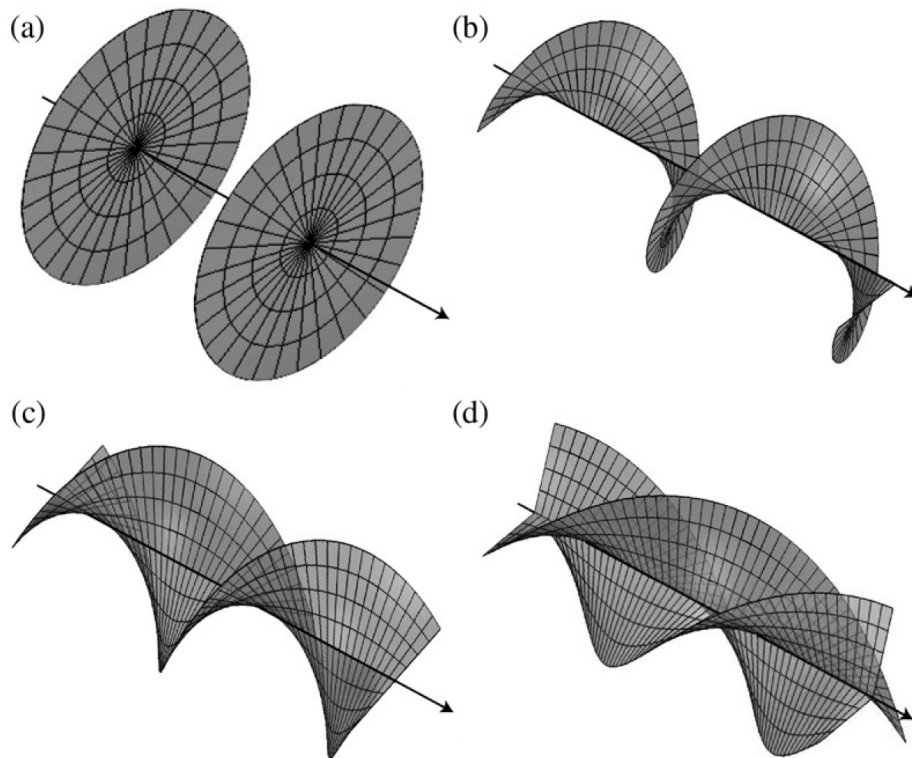


Figure 1.1: Illustration of wavefronts for (a) $l = 0$, (b) $l = 1$, (c) $l = 2$, (d) $l = 3$. Taken from [6].

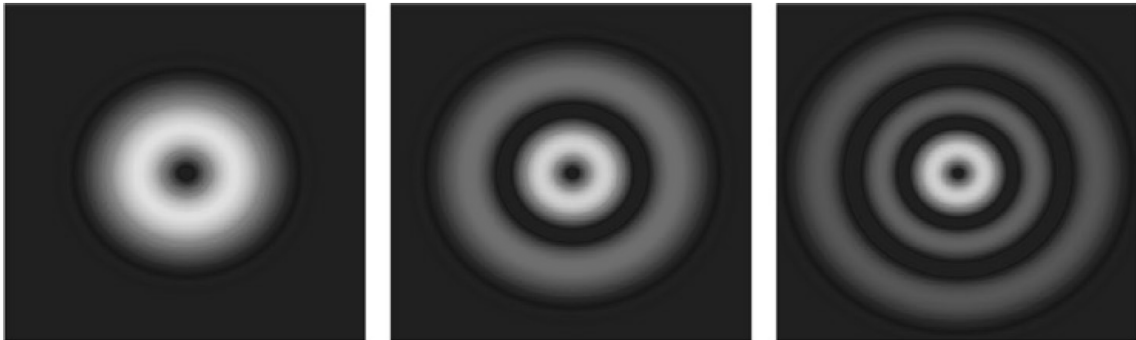


Figure 1.2: Intensity profiles of modes LG_0^1 , LG_1^1 , LG_2^1 , respectively. Adapted from [6].

1.3 OAM generation

Our knowledge about OAM would not be complete without a discussion about its generation, manipulation and detection. This list of techniques will later be used as a guideline on what operations with OAM (and other degrees of freedom) of a photon are possible.

The most intuitive method to produce a beam with a phase $\exp(il\varphi)$ is to take advantage of a special phaseplate which simply adds the desired term. Normal phase retarders shift the phase of an incident beam by a set amount, but it is possible to create a plate whose phase-shift is dependant on position. In our case, the goal is to produce helically phased beam, which can be achieved, for example, by a plate with in a spiral varying thickness [16] as illustrated in Fig.1.3. The simplicity of the idea is nevertheless outweighed by several disadvantages resulting in a sparse use of spiral phaseplates in practice. Firstly, such a device is extremely difficult to manufacture due to high precision requirements. Secondly, even though there exists a tunable spiral phaseplate [17], the height of the step (h in Fig.1.3) depends on the wavelength and cannot be used universally.

On the other hand, mode converters are used in practice commonly. Ordinary lasers can be easily adjusted to operate with a rectangular symmetry, which leads to oscillations in Hermite-Gaussian (HG) modes [11, p. 648]. HG modes form another complete set of solutions to the paraxial equation and therefore it is possible to express any beam in either HG or LG basis. The idea behind mode converters is then to shift a phase of several HG modes in order for their sum to be equal to a LG mode. Conveniently, such transformation can be performed with only a pair of cylindrical lenses [18].

On a completely different principle operate so called q-plates [19]. It is well known that circularly polarized beams carry a spin orbital momentum (SAM) equal to $\pm\hbar$ per photon. Q-plates are constructed from a birefringent material with a position dependent optical axis that can manipulate the SAM, see Fig.1.4. Plates with rotational symmetry are able to switch the orientation of circular polarization of a passing photon and consequently give the photon an orbital angular momentum to balance the difference. For example, a left-circular photon with a planar wavefront is converted to right-circular, i.e. SAM changes as $+\hbar \rightarrow -\hbar$, and additionally gains OAM equal to $2\hbar$. Note that some other designs without symmetric configurations of optical axes (case (a) in Fig. 1.4) do not preserve the total angular momentum and, while they still reverse the polarity of SAM, part of the angular momentum is transferred to the q-plate.

The last method presented here are forked diffraction gratings. Either the binary gratings or the phase modulators (discussed later) are the preferred choice of generating helical beams

for many scientists, mostly thanks to their versatile implementation on computer generated holograms [20]. The devices are programmed with a pattern calculated as interference fringes of the desired beam with a reference wave. Figure 1.5 shows an example of an interference image between a plane wave and a beam in LG_0^1 mode. In an optical setup, such hologram would be illuminated with a plane wave producing two diffracted beams $LG_0^{\pm 1}$ in the first order (to the left and right). Naturally, there are other uninteresting orders of diffraction (e.g. LG_0^0 in the 0th), which take away some of the total intensity [2, p. 313].

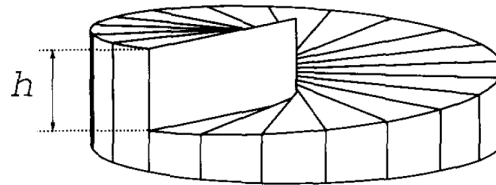


Figure 1.3: Spiral phase plate with step height h . Taken from [16].

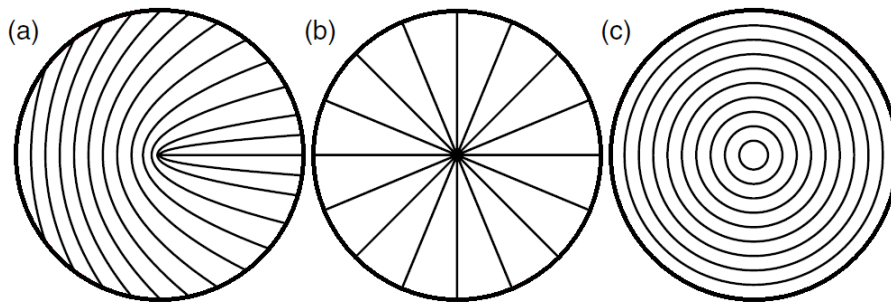


Figure 1.4: q-plates, where the thin lines indicate the direction of the optical axis. Design (a) does not convert the angular momentum perfectly and a part is transferred to the plate. (b) and (c) are rotationally symmetric and preserve the total angular momentum. Taken from [19].

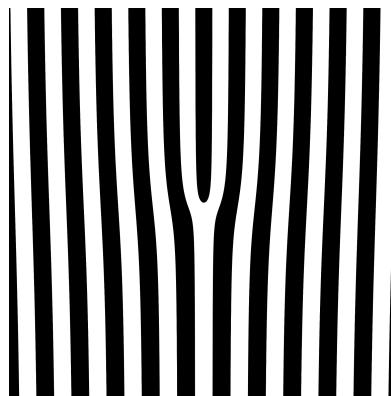


Figure 1.5: Diffraction pattern between a plane wave and LG_0^1 mode.

1.4 OAM manipulation

Having obtained a beam with OAM, it is now desired to manipulate the LG modes. Although LG beams with different radial indices p are of some interest [20], our research is focused on operations with the azimuthal index l .

To follow up on the last paragraph, the binary forked gratings suggest a resourceful utilization of higher diffraction orders. Intuitively speaking, the described process can be performed in reverse by illuminating the grating with an LG mode and obtaining a plane wave in the zeroth order as well as other modes in higher orders. Indeed, a beam with a phase $\exp(il\varphi)$ passing through a grating with Δm dislocations (example Fig.1.5 has $\Delta m = 1$) would be split into different modes, where the n th diffraction order would acquire a phase $\exp(i(l + n\Delta m)\varphi)$ [7]. Since it is possible to improve the efficiency of a grating by blazing it to diffract the most into the first order, well-performing optical elements that increase (or decrease) OAM of a beam by $\Delta l = \Delta m$ are readily available [8].

Alternatively, instead of a simple binary grating one could use a spatial phase modulator with a continuous phase change to alter the OAM. Such a device can be programmed with an arbitrary phase profile, for example a helical one given by $e^{i\delta\varphi}$. A beam, which already had a phase expressed as $e^{il\varphi}$, passing through, or reflected off, the hologram would leave it with OAM equal to $(l + \delta)\hbar$ [6]. (In practice, the hologram usually contains a sum of the helical phase along with a linear phase ramp directing the beam in different direction, as illustrated in Fig.1.6.) The terms like hologram, $\pm\delta$ -modulator or filter $F_{\pm\delta}$ used throughout the text will refer to this kind of operation.

The previous method is, in a sense, addition of a constant δ to the value l . To expand our set of arithmetic operations with OAM, we also need an ability to multiply (or divide) it. Due to the fact that OAM is solely determined by the phase term $\exp(il\varphi)$, we propose a coordinate transformation $\varphi \rightarrow \varphi/n$, which essentially multiplies the OAM by n . The division of l would be performed by the transformation $\varphi \rightarrow n\varphi$, but only for values divisible by n (otherwise the result would be a combination of LG modes without a defined OAM). In most cases, coordinates can be transformed using phase modulators with a programmable filter to stretch, rotate or variously modify an image [21]. Details about realizability of general transformations were discussed in our previous work [22], here we focus only on the two simple cases, multiplying or dividing OAM by 2, which will be useful for our forthcoming algorithms.

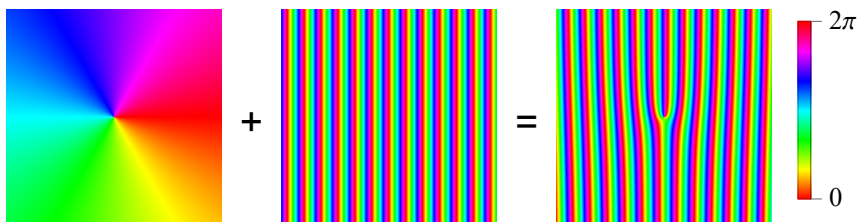


Figure 1.6: Programming a computer generated hologram with a helical phase $e^{i\delta\varphi}$ (in this case $\delta = 1$) and a linear phase ramp $e^{i\beta x}$ (for some small angle β) at the same time creates a forked spatial phase modulator. A beam passing through this optical element gains a phase $e^{i\delta\varphi+i\beta x}$, which changes its OAM and the direction of propagation.

The proposed $\times 2$ -modulator consists of a conventional lens L and two filters, Φ (transformation) and Ψ (phase correction), in each focal plane, as illustrated in Fig.1.7. The symbol “ $\times 2$ ” refers to the operation performed on the OAM and should not be confused with the coordinate transformation, which in this case is halving the azimuthal angle $\varphi \rightarrow \varphi/2$. For this transformation we already calculated (in Cartesian coordinates) the corresponding phase profile in [22]

$$\tilde{\Phi}_{(\times 2)}(x, y) = \exp \left[-i \frac{k}{f} \frac{\sqrt{2}}{3} \left(\sqrt{x^2 + y^2} - 2x \right) \sqrt{\sqrt{x^2 + y^2} + x} \right], \quad (1.10)$$

where k is the wave number and f is the focal length of the lens L . The effect of the $\tilde{\Phi}_{(\times 2)}$ on an incoming LG_0^1 beam (Fig.1.8a)) is modelled in Fig.1.8b). Here the transformed image is displayed in the second Fourier plane already after the appropriate phase correction by the function

$$\Psi_{(\times 2)}(x, y) = \exp \left[i \frac{k}{f} \left(\frac{x^3}{3} - xy^2 \right) \right] \quad (1.11)$$

calculated from the inverse transformation [22]. As can be seen, only a half of the beam is created (since halving all angles in a circle produces a half-circle). To gain the correct output we need to somehow generate another half-circle rotated π radians (i.e. Fig.1.8c)) and combine both to obtain the full beam. One possible method, to be referred to as method A, is to modify the amplitude along with the phase of the incoming beam. If any phase-amplitude spatial modulators are available, it is easy to calculate the proper function they should be programmed with, since the rotated half-beam from Fig.1.8c) can be created simply by the complex conjugated profile $\tilde{\Phi}_{(\times 2)}^*$. From linearity it follows that the equal-weight superposition of the two profiles

$$\Phi_{(\times 2)}(x, y) = \frac{1}{2} \left(\tilde{\Phi}_{(\times 2)} + \tilde{\Phi}_{(\times 2)}^* \right) = \text{Re} \left(\exp \left[-i \frac{k}{f} \frac{\sqrt{2}}{3} \left(\sqrt{x^2 + y^2} - 2x \right) \sqrt{\sqrt{x^2 + y^2} + x} \right] \right), \quad (1.12)$$

produces a sum of the two outputs, which we modelled in Fig.1.8d). Transformation of several higher order LG modes can be seen in Fig.B.1 and Fig.B.2 in the Appendix. The higher the azimuthal number, the stronger deformation effects can be observed and the worse resemblance the beam has in comparison with its untransformed counterpart LG_0^{2l} . Another drawback of the amplitude modulation is the reduced throughput, in this case responsible for more than 50% loss of intensity. Detailed discussion about differences between the transformed beams and the targeted LG_0^{2l} is provided in Chapter 4.

The $/2$ -modulator of method A could be intuitively implemented by inverting the process described above. Having reversed the order of the filters from the previous case, the setup is again the same as in Fig.1.7, but with the input filter

$$\Phi_{(/2)}(x, y) = \exp \left[i \frac{k}{f} \left(\frac{x^3}{3} - xy^2 \right) \right] \quad (1.13)$$

and the phase-amplitude modulator

$$\Psi_{(/2)}(x, y) = \text{Re} \left(\exp \left[-i \frac{k}{f} \frac{\sqrt{2}}{3} \left(\sqrt{x^2 + y^2} - 2x \right) \sqrt{\sqrt{x^2 + y^2} + x} \right] \right), \quad (1.14)$$

which functions as the corrector. Transformation of a test beam LG_0^2 (Fig.1.9a)) right after $\Psi_{(/2)}$ is modelled in Fig.1.9b). Although the result does not resemble any LG mode, upon

further propagation the interference fringes leave the central part and an almost-correct beam is restored. The plots c) and d) in Fig.1.9 show the beam from b) after travelling 1/2 and 1 Rayleigh range, respectively. Nevertheless, some interference fringes can still be seen in c) moving away from the center which contribute to a severe loss of energy. The total intensity in d) is again less than 50% of the transformed beam b) before propagation. For this reason we abandon the simple but inefficient inversion of modulators and try a different method.

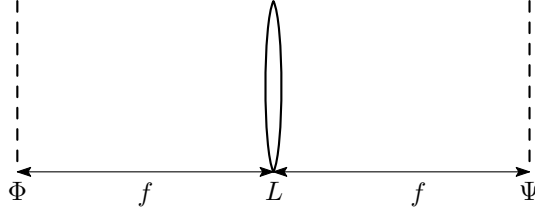


Figure 1.7: Single lens setup of method A to perform a coordinate transformation given by a modulator Φ and a phase corrector Ψ .

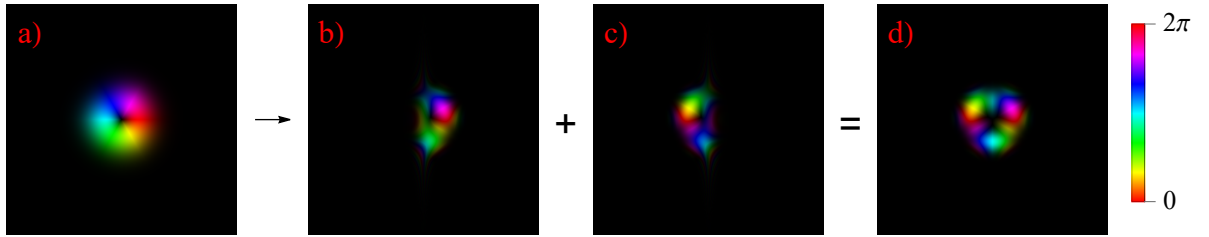


Figure 1.8: Modelled phase profiles of LG_0^1 mode $\times 2$ -transformation, method A. a) Input beam right before first modulator Φ . b) and c) The beam transformed by $\tilde{\Phi}_{(\times 2)}$ and $\tilde{\Phi}_{(\times 2)}^*$, respectively, in the second focal plane after phase correction by $\Psi_{(\times 2)}$. d) The final output beam with doubled phase variance (after Ψ) created by the phase-amplitude modulator $\Phi_{(\times 2)}$. Brightness is adjusted for illustration purposes. Description of our numerical simulations is provided in the Appendix.

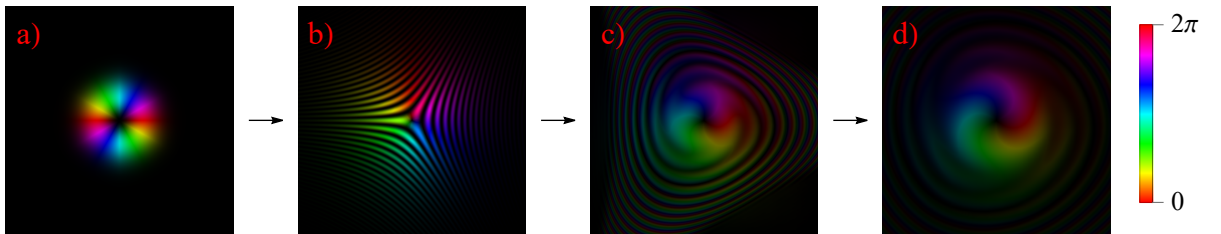


Figure 1.9: Modelled phase profiles of LG_0^2 mode $/2$ -transformation, method A. a) Input beam right before the first modulator $\Phi_{(/2)}$. b) The transformed beam right after the correcting phase-amplitude modulator $\Psi_{(/2)}$. c) The result from b) propagated over distance of 1/2 Rayleigh range. Observe the ripples carrying away approximately 50% of intensity. d) The reconstructed beam after 1 z_R .

To improve the efficiency, we suggest a different scheme to halve OAM, which we call method B. The main idea for $/2$ -modulation of the design illustrated in Fig.1.10 is to split the incoming beam into two parts, essentially creating two half-circles and then modulating each part separately before recombining them. The modulator

$$\hat{\Phi}_{(/2)}(x, y) = \begin{cases} \Phi_{(/2)}(x, y) \exp\left(i\frac{k}{f}\beta y\right), & \text{if } x \geq 0 \\ \Phi_{(/2)}(-x, y) \exp\left(-i\frac{k}{f}\beta y\right), & \text{if } x < 0 \end{cases} \quad (1.15)$$

performs both actions, splitting and modulating, at the same time, with the parameter β representing the small angle of vertical deviation in the linear phase ramp. Note that each half can be directed independently by multiplying it by the expression $\exp[ik/f(\beta_x x + \beta_y y)]$ [22]. Fig.1.11b) shows the separated beams in the Fourier plane, where both can enter their own phase corrector

$$\begin{aligned} \hat{\Psi}_{(/2)}^{(x \geq 0)}(x, y) &= \tilde{\Phi}_{(\times 2)}(x, y) \exp\left(-i\frac{k}{f}\beta y\right), \\ \hat{\Psi}_{(/2)}^{(x < 0)}(x, y) &= \tilde{\Phi}_{(\times 2)}(-x, y) \exp\left(i\frac{k}{f}\beta y\right). \end{aligned} \quad (1.16)$$

(The upper index does not suggest a restriction of the domain.) The beams before and after correction are plotted in Fig.1.11 c), c') and d), d'), respectively. Both of them now approximate the targeted $LG_0^{l/2}$, but one is rotated 180° with respect to the other. Therefore, a beam rotator ((\odot_π) , i.e. with $\alpha = \pi$) is inserted in one arm correcting the difference for beams with odd $l/2$ and leaving beams with even $l/2$ unchanged. Finally, a beam splitter sends the sum of both beams to one output (Fig.1.11e)) and the difference to the other (Fig.1.11f)). (For more details, see the next section where the function of the beam rotator and the beam splitter will be justified with calculations.) Transformed phase profiles of some higher order LG modes are modelled in Fig.B.3, Fig.B.4 right after recombination as well as after propagating.

Like before, reversing the scheme in Fig.1.10 essentially performs the inverse operation, i.e. the OAM multiplication. The Fig.1.12 shows both halves, b) and c), of the split beam after the transformation, as well as their sum d). Compared to the method A (Fig.1.8), $\times 2$ -modulation of method B takes more of a rectangular shape, instead of triangular. The reason is the difference of the modulators defined by the equation (1.16), which are mirrored to each other.

Even though no loss of intensity is observed, a great disadvantage of method B is its complexity and high sensitivity to precise alignment. A thorough examination of realizability of both methods will be given in the last chapter.

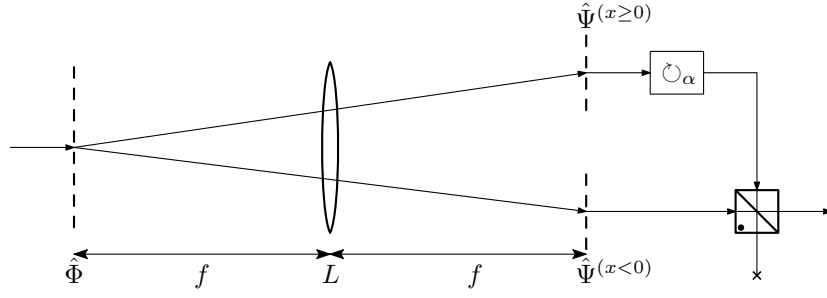


Figure 1.10: Schematic illustration of method B to halve OAM. The filter $\hat{\Phi}_{(1/2)}$ splits and modulates the incoming beam, which is then transformed through a lens L , similarly as in Fig.1.7. The beams are spatially separated and each can enter their own phase corrector $\hat{\Psi}_{(1/2)}$. One beam is then rotated by the angle α before recombining both arms on a beam splitter.

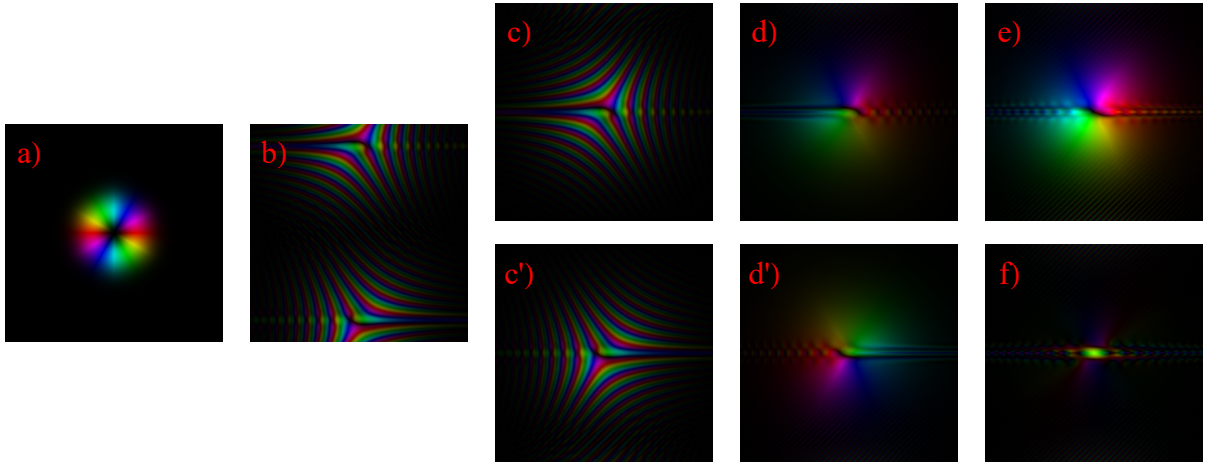


Figure 1.11: Phase profiles of modelled passage of LG_0^2 through the different stages in the setup in Fig.1.10. a) Input beam right before the modulator $\hat{\Phi}_{(1/2)}$, which also splits the beam in half. b) Separated beams in the Fourier plane of the lens. c), c') The same as in b) right before phase correction, but drawn separately and centered. d), d') Beams corrected by $\hat{\Psi}_{(1/2)}$. e), f) Outputs of the beam splitter (after rotation in one arm) where constructive and destructive interference is observed, respectively.

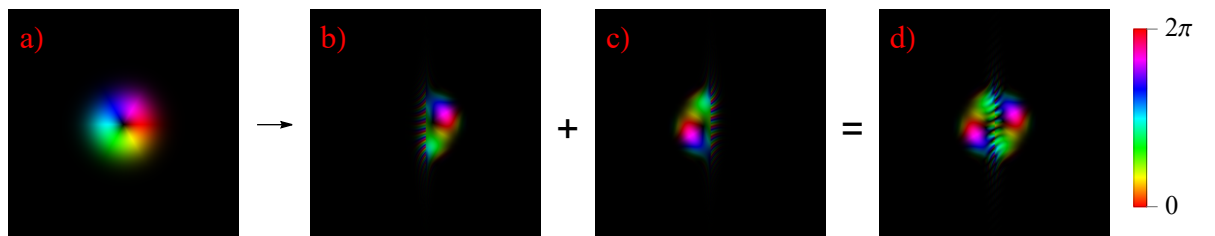


Figure 1.12: Modelled phase profiles of LG_0^1 mode $\times 2$ -transformation method B performed with reversed setup in Fig.1.10. a) Input beam. b) and c) The result of the transformation, if only one of the modulators defined in (1.16) were present, respectively. d) The final output beam combined from b) and c).

1.5 OAM detection

Detection of OAM completes the basic introduction to this topic. Again, leading up to sections about bitwise manipulation, we focus only on some special methods useful for future discussion.

One possibility to check whether a beam is in a specific mode is to send it through a corresponding forked hologram and measure the intensity in the first order. In cases where the value l of the beam and the hologram match, the single mode fibre detector registers distinguishably more intensity than if the values differ [6, 7, 23].

Another method is to observe the distinctive interference patterns, for example like in Fig.1.5. Although counting dislocations in a fork pattern is reliable and common experimental technique [14, 2, 17, 19, 20], it is not suitable for our purposes. We would like to make an operation with the beam specific to its OAM, e.g. to distinguish between beams with even and odd value of the OAM.

Such a parity sorter of OAM (capable of handling even single photons) can be implemented in a Mach-Zehnder interferometer with clever use of a beam rotator [24, 25]. In principle, beams with “circular symmetry” in a form of the phase factor $\exp(il\varphi)$ have a property that a rotation by an angle α is the same as shifting the phase by $l\alpha$. The interferometer can use, for example, two Dove prisms (with respective angle $\alpha/2$ as seen in Fig.1.13) to change the relative angle between the beams in each arm and then let them constructively or destructively interfere on the output beam splitter. Expressed mathematically, a general beam $u(r)\exp(il\varphi)$ is split equally into two paths on the first beam splitter and in one arm, say B , the beam gains the additional phase $\exp(il\alpha)$, while in A it stays unchanged

$$\begin{pmatrix} A \\ B \end{pmatrix} = \frac{1}{\sqrt{2}} \begin{pmatrix} u(r)e^{il\varphi} \\ u(r)e^{il\varphi}e^{il\alpha} \end{pmatrix}. \quad (1.17)$$

On the second 50/50 beam splitter the two paths are combined resulting in [8]

$$\begin{pmatrix} C \\ D \end{pmatrix} = \frac{1}{\sqrt{2}} \begin{pmatrix} 1 & 1 \\ 1 & -1 \end{pmatrix} \begin{pmatrix} A \\ B \end{pmatrix} = \frac{1}{2}u(r)e^{il\varphi} \begin{pmatrix} 1 + e^{il\alpha} \\ 1 - e^{il\alpha} \end{pmatrix}. \quad (1.18)$$

To sort beams by parity of l , an angle $\alpha = \pi$ is introduced. Beams with even l interfere constructively on output C , while odd-valued beams exit through port D .

It is important to note, that the device manages to sort beams in an arbitrary superposition state of LG modes. Moreover, this method can be adapted to distinguish between all positive values of l by cascading multiple sorters in a sequence with an appropriate angle α [24]. The first stage is a parity sorter with $\alpha = \pi$ as above. In the second stage, even- l beams enter another sorter with $\alpha = \pi/2$, which separates values $l = 4k$ from $l = 4k + 2$. On the other hand, beams with odd l cannot be sorted immediately, since there is no appropriate rotation angle. They are first transformed into even valued by increasing their l by one (for example by forked diffraction gratings). Then they can be sorted similarly to the even- l beams by an additional interferometer with $\pi/2$. Finally, the output of the second stage are four channels each corresponding to l in one of the congruence classes, i.e. $l = 4k, 4k + 1, 4k + 2, 4k + 3$. Further sorting in third stage would require 4 more interferometers with the angle $\alpha = \pi/4$ and some holograms to adjust two of the beams, as is illustrated in Fig.1.14.

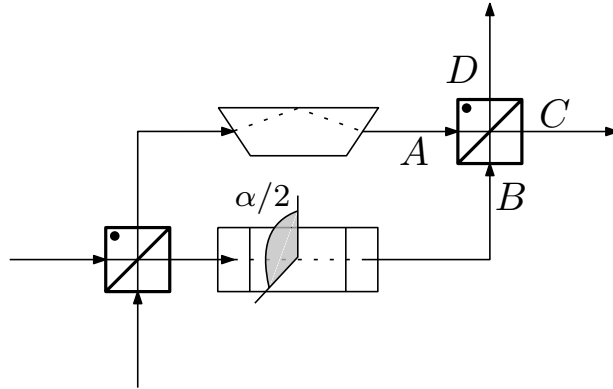


Figure 1.13: Parity sorter made from a Mach-Zehnder interferometer with two Dove prisms acting as beam rotators. The relative angle between the Dove prisms is $\alpha/2$.

Alternatively, instead correcting the beams with “problematic” l with holograms, an additional phase shifter could be introduced in one arm of the appropriate interferometer [25]. For example, odd l beams in the second stage entering the interferometer (without going through holograms) are to be sorted into two groups: $(l \bmod 4) = 1$ and $(l \bmod 4) = 3$. Rotating the beams by relative angle $\alpha = \pi/2$ introduces a phase shift $\Delta\phi_\alpha^{(1)} = l\alpha = (4k+1)\pi/2 = 2\pi k + \pi/2 \cong \pi/2$ and $\Delta\phi_\alpha^{(2)} = l\alpha = (4k+3)\pi/2 = 2\pi k + 3\pi/2 \cong 3\pi/2$ to the first and second group, respectively (the integer multiple of 2π is irrelevant). If the beams were combined like this on the output beam splitter, no constructive or destructive interference would be observed, since beams from neither of the groups are in (or out) of phase from their unrotated counterpart. However, by adding a constant (l -independent) phase shift $\Delta\phi_c = -\pi/2$, the total phase difference between the beams in the two arms becomes $\Delta\phi^{(1)} = \Delta\phi_\alpha^{(1)} + \Delta\phi_c = 0$ and $\Delta\phi^{(2)} = \Delta\phi_\alpha^{(2)} + \Delta\phi_c = \pi$, both groups fully constructively or destructively interfere and each leaves the interferometer through its own output channel.

First three stages of a complete sorter are illustrated in Fig1.15. The constant phase (in the n th stage) is calculated from the formula $\Delta\phi_c = -m\alpha$, where $(l \bmod 2^{(n-1)}) = m$ corresponds to the congruence class sorted in the previous stage. In conclusion, this alternative method may be more challenging to construct (each interferometer requires an individually tuned phase shift), but does not employ inefficient holograms and thus is more suitable for single photon sorting [25].

Ultimately, a simpler device can be used in case only a small set of different OAM beams is to be sorted. The idea is based on coordinate transformations and comes from the article [26], which served as one of the main sources of inspiration for our OAM modulators. The central element of this method is a hologram programmed with

$$\Phi(x, y) = \exp \left[i \frac{k}{f} \left(y \arctan\left(\frac{y}{x}\right) - x \ln\left(\sqrt{x^2 + y^2}\right) + x \right) \right] \quad (1.19)$$

to perform log-polar to Cartesian coordinate transformation

$$\begin{pmatrix} x \\ y \end{pmatrix} \rightarrow \begin{pmatrix} -\ln\left(\sqrt{x^2 + y^2}\right) + x \\ \arctan\left(\frac{y}{x}\right) \end{pmatrix} \quad (1.20)$$

between two focal planes of a lens in the configuration of Fig.1.7. Concentric rings with varying azimuthal phase of multiples 2π (in the object plane) display as parallel lines in position

depending on the azimuthal number l (in the image plane). As before (in case of the $\times 2$ - and $/2$ -modulators), another hologram

$$\Psi(x, y) = \exp \left[-i \frac{k}{f} e^{-x} \cos y \right] \quad (1.21)$$

is included in the output to correct the phase distortion caused by different optical path lengths.

It was experimentally demonstrated that the optical device can reliably sort OAM beams from $l = -5$ to $l = 5$, and even determine if the beam is in superposition of two modes LG_0^{-1} and LG_0^2 [26]. However, the larger the azimuthal number, the more the neighbouring detection zones overlap and the harder it is to distinguish between them.

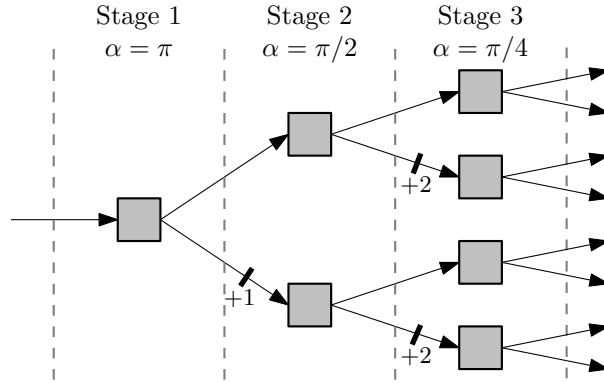


Figure 1.14: First 3 stages of the OAM sorter made from a Mach-Zehnder interferometer sorters (gray boxes) like in Fig.1.13 and a few holograms (“+1” and “+2”).

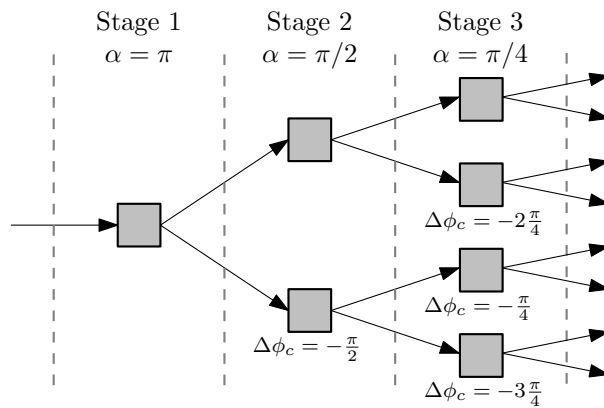


Figure 1.15: OAM sorter similar to Fig.1.14. Instead of holograms, some interferometers contain phase shifter introducing constant phase shift $\Delta\phi_c$ in one arm.

Chapter 2

Classical logic operations with OAM

Equipped with many techniques for handling beams with OAM, we are ready to proceed to the first topic of this thesis, classical logical operations. The idea to use OAM states as carriers of information arose from the realization at the end of Section 1.2, where we discussed orthogonality of LG modes. Additionally, the azimuthal number l is principally unbounded and therefore suitable for representing an arbitrarily long string of bits.

Take a binary number, for example $(\dots xyz)$, where $x, y, z \in \{0, 1\}$. Such a string naturally represents a decimal number l in base 2

$$l = (\dots xyz)_2 = \dots + x \cdot 2^2 + y \cdot 2^1 + z \cdot 2^0. \quad (2.1)$$

Now any bitwise operation on $(\dots xyz)$ can be viewed as some arithmetic operation with its representative l . However, since our OAM manipulation capabilities are limited, we will only focus on few simple cases. The first section presents the right shift of a string and the associated last bit extraction. The left shift is described in the second section, followed by an explanation of injecting information into the last bit. As an application of the right and left shifts, the third section contains an example utilizing both methods. The last section introduces a new notation to more easily describe optical systems with parity sorters and shifters.

2.1 Right shift

First we take a look at implementation of right bit shift. Two illustrative examples are

$$\begin{aligned} (0010) &\rightarrow (0001), \\ (0101) &\rightarrow (0010). \end{aligned} \quad (2.2)$$

Only the last 4 digits are expressed here, because we assume that there are infinitely many zeros to the left and we omit most of them. At the end of the number, the right shift destroys the last bit and we lose the information stored in it.

In the decimal representation, this bitwise operation could be replaced with simple division by two. Generally, to shift all bits of a string (xyz) one position over to the right is equivalent to lowering the exponents by one in its decimal expansion

$$x \cdot 2^2 + y \cdot 2^1 + z \cdot 2^0 \rightarrow x \cdot 2^1 + y \cdot 2^0. \quad (2.3)$$

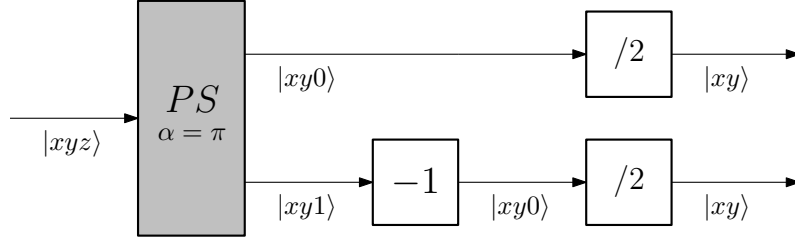


Figure 2.1: Conceptual diagram for performing the right shift. Information from the lost bit is converted into position.

Of course, there is a problem with odd numbers, since they are not divisible by two. We propose a solution, which incorporates the previous issue about the “lost” information.

The idea is, that parity of a number is decided by the last digit in its binary expansion. If we separate even and odd numbers, each group will have the same last bit and can be operated on individually. The implementation with the OAM modes could look like in Fig.2.1. A string (xyz) is now represented by a beam in a state $|xyz\rangle$, where $l = (xyz)_2$ is its azimuthal number. The beam first enters a parity sorter (PS), which sends even-valued beams through the top channel and odd- l beams through the bottom channel. The separation effectively reads the last bit of the string (xyz) and converts that information into position: $z = 0$ corresponds to the top path, $z = 1$ to the bottom path. After that, the even- l beam is transformed by a phase modulator (box labelled “/2”, for details refer to Section 1.4) into $l/2$ -valued beam, whereas the bottom beam goes through a hologram prior to the phase modulation. The hologram (illustrated as “-1”) could be a forked grating, which diffracts the beam into the first order with decreased azimuthal number by one. Undoubtedly, the bottom beam now has an even l and its value can be halved by another /2-modulator without a problem. As a result, the beam leaves the right-shifter in a state $|xy\rangle$ through one of the output channels, carrying the information from the z bit as its position.

It is important to add, that the property of a parity sorter to handle beams in superposition carries over to the right shifter. Any combination of bit strings in the input (for example a beam made out of two LG modes representing $|uvw\rangle + |xyz\rangle$) correctly shifts and leaves through the appropriate output as $|uv\rangle + |xy\rangle$ if $w = z$, or $|uv\rangle$ in one output and $|xy\rangle$ in the other if $w \neq z$.

2.2 Left shift

Following up, naturally, is the left shift of a bit string. By shifting all bits one position to the left a vacant space is made at the end, which needs to be somehow filled. Since the previously discussed right shift already stores information in position, it would be convenient to decide the last bit again based on position of the beam. This way both of the devices would be compatible and naturally perform inverse operations.

The proposed design is schematically illustrated in Fig.2.2a). The input are two channels, the top one corresponding to the operation “append 0” and the bottom one to “append 1”. A beam in either input first goes through a phase modulator (element labelled “ $\times 2$ ” operating according to the Section 1.4) which doubles the value of its OAM. The resulting state propagates unchanged further in the top path, while in the bottom path it is diffracted by a hologram (“+1”) which appends 1 to the bit string. Both beams are then combined by an inverted parity sorter (PS^\dagger) and leave the device as a sum through a single output channel.

Moreover, the two input beams do not even have to be the same, as we will explain. The action of inverted parity sorter can be mathematically expressed following similar steps as in Section 1.5. Conversely, we use a simplified diagram in Fig.2.2b) of Mach-Zehnder interferometer with differently labelled arms and an arbitrary beam rotator (\odot_α). Leave, for a moment, the bit notation and write the two input beams as $|uv\rangle = f(r) \exp(ik\varphi)$, $|xy\rangle = g(r) \exp(il\varphi)$. Thus the beams entering the PS^\dagger after the appropriate transformations are

$$A = f(r)e^{i2k\varphi} \quad \text{and} \quad B = g(r)e^{i(2l+1)\varphi}. \quad (2.4)$$

The first beam splitter combines inputs A , B and sends the result into two arms

$$\begin{pmatrix} C \\ D \end{pmatrix} = \frac{1}{\sqrt{2}} \begin{pmatrix} 1 & 1 \\ 1 & -1 \end{pmatrix} \begin{pmatrix} A \\ B \end{pmatrix} = \frac{1}{\sqrt{2}} \begin{pmatrix} f(r)e^{i2k\varphi} + g(r)e^{i(2l+1)\varphi} \\ f(r)e^{i2k\varphi} - g(r)e^{i(2l+1)\varphi} \end{pmatrix}. \quad (2.5)$$

Then the beams are rotated with respect to each other by an angle α , for example by a pair of Dove prisms (each arm by $\alpha/2$, see Fig.1.13) or by a single beam rotator (\odot_α) in one arm and nothing in the other. Rotating the circularly symmetric beam introduces a phase proportional to its azimuthal number

$$D' = (\odot_\alpha)D = \frac{1}{\sqrt{2}} \left(f(r)e^{i2k(\varphi+\alpha)} - g(r)e^{i(2l+1)(\varphi+\alpha)} \right). \quad (2.6)$$

The second beam splitter operates the same way as the first one, we only have to pay attention to the order of the input beams

$$\begin{pmatrix} E \\ F \end{pmatrix} = \frac{1}{\sqrt{2}} \begin{pmatrix} 1 & 1 \\ 1 & -1 \end{pmatrix} \begin{pmatrix} D' \\ C' \end{pmatrix} = \frac{1}{2} \begin{pmatrix} f(r)e^{i2k(\varphi+\alpha)} - g(r)e^{i(2l+1)(\varphi+\alpha)} + f(r)e^{i2k\varphi} + g(r)e^{i(2l+1)\varphi} \\ f(r)e^{i2k(\varphi+\alpha)} - g(r)e^{i(2l+1)(\varphi+\alpha)} - f(r)e^{i2k\varphi} - g(r)e^{i(2l+1)\varphi} \end{pmatrix}. \quad (2.7)$$

Finally, with the choice of $\alpha = \pi$, the output F vanishes and E becomes

$$\begin{aligned} E &= \frac{1}{2} \left(f(r)e^{i2k\varphi} \cdot 1 - g(r)e^{i(2l+1)\varphi} \cdot (-1) + f(r)e^{i2k\varphi} + g(r)e^{i(2l+1)\varphi} \right) \\ &= f(r)e^{i2k\varphi} + g(r)e^{i(2l+1)\varphi} \\ &= |uv0\rangle + |xy1\rangle, \end{aligned} \quad (2.8)$$

i.e. the output is a combination of beams, where the one from the top input has 0 added at the end while the beam from the bottom input gains 1 at the end of its bit representation.

2.3 Example: swap of the last 2 bits

The two simple operations presented here can be chained one after the other to perform more complex bitwise operations with a single string. An example would be swapping the last two bits, that is $|xyz\rangle \rightarrow |xzy\rangle$. Conceptual diagram of the correct arrangement of right and left shifters is shown in Fig.2.3.

Even though the device works on beams in superposition, it is most easily understood on a few simple cases. Take the input state $|x01\rangle$. The first right shift reads the 1 at the end and sends the beam on the bottom path as $|x0\rangle$. The second right shifter translates the last 0 into position (third path between the right and left side) and the beam becomes only $|x\rangle$. Now, with the value of the last two bits encoded in position, the set of left shifters needs to correctly decode each path back to bit representation. By sending the third output channel from the right shifters

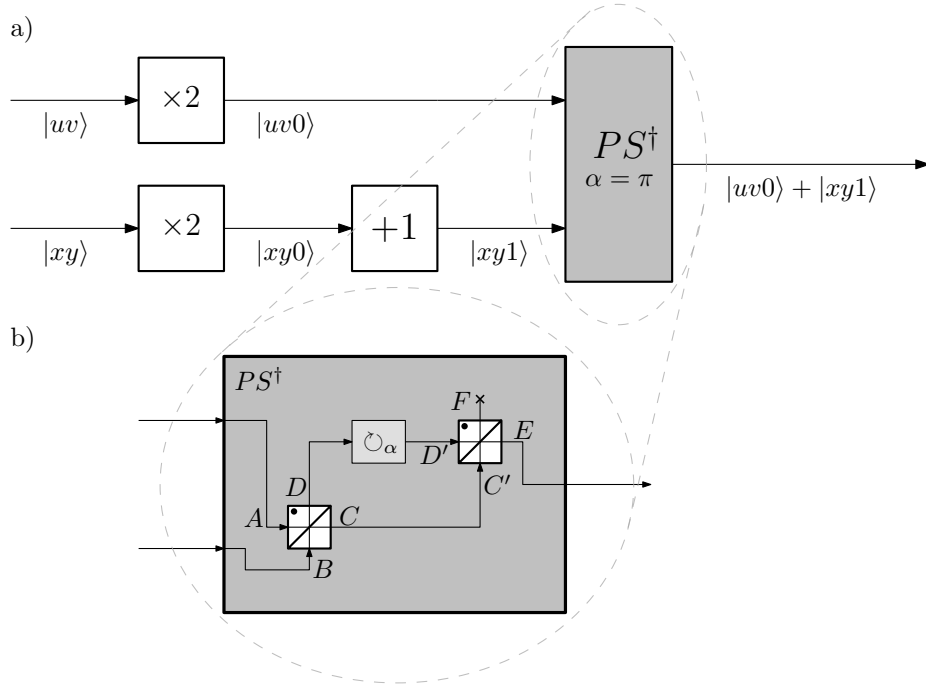


Figure 2.2: a) Diagram of left shifter. Bit string entering through the top channel has 0 added at the end, while the bottom input represents addition of 1 at the end. b) Details of inverted parity sorter PS^\dagger consisting of Mach-Zehnder interferometer with two beam splitters (white boxes) and a beam rotator (\mathcal{C}_α) in one arm.

into the second input of the left shifters we perform the swap $(01) \rightarrow (10)$ and can transform the beam $|x\rangle$ first into $|x1\rangle$ (it entered through the bottom channel, which is equivalent to adding 1 at the end) and then into $|x10\rangle$ (top input of left shifter corresponds to adding 0).

On the other hand, the state $|x00\rangle$ follows a simpler path. The device has to recognise the two 0s at the end (which do not have to be swapped) and send the beam to the output unchanged.

Although the 2 bit swap in Fig.2.3 nicely illustrates cascading possibilities of both shifters, a much simpler device can perform this particular operation. To swap two last bits in a string, no shifting is necessary, we only need to distinguish between the 4 possible combinations of the bits. The main idea takes inspiration from articles [27, 28], where a different operation (cyclic permutation of states $|l\rangle$) is broken down into three stages: separation of OAM states, operation with individual channels and recombination.

The device in Fig.2.4 is essentially twice the first two stages of the improved OAM sorter from Fig.1.15, one mirrored. The left side only sorts beams into congruence classes of their azimuthal number (as described in Section 1.5). In the binary representation, these classes correspond to the last bits (00), (01), (10), (11) and, once separated, we can operate with the individual pairs of bits by manipulating the 4 channels. In case the last two bits are identical (i.e. (00) or (11)), no action is required and both paths proceed to the combiner (right side with inverted sorters PS^\dagger) unchanged. On the contrary, the middle two channels are affected by the swap and, beside interchanging positions, they also go through “ ± 1 ” hologram to be correctly recombined.

Operation of all the parts from the Fig.2.4 has been already explained (since they act similarly), but at least one piece could be discussed here in greater detail. The most complicated

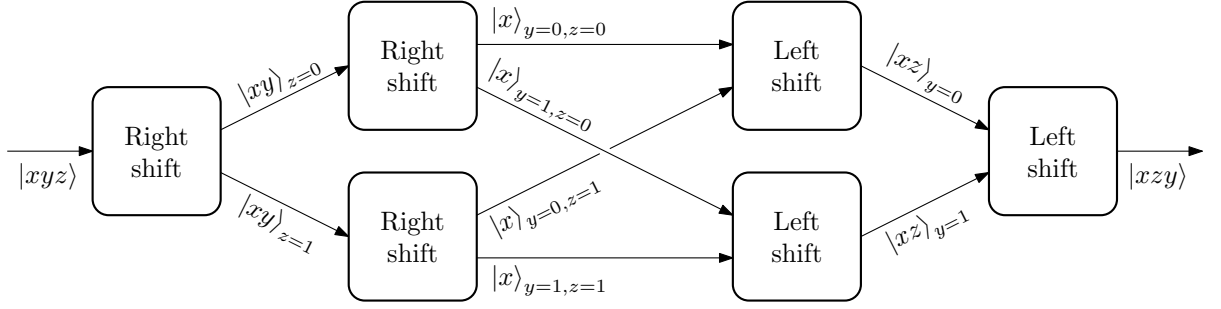


Figure 2.3: Scheme to perform swap of the last two bits. Input beam representing bit string $|xyz\rangle$ is transformed by a set of right and left shifters into $|xzy\rangle$.

one is probably the inverted sorter with additional phase ($PS_{\alpha=\pi/2, \Delta\phi_c=-\pi/2}^\dagger$) which can be mathematically described following the same steps from the previous section with few crucial differences. Firstly, the two input beams A and B need their azimuthal numbers to be in the correct congruence class (i.e. end with (01) and (11))

$$A = f(r)e^{i(4k+1)\varphi} \quad \text{and} \quad B = g(r)e^{i(4l+3)\varphi}. \quad (2.9)$$

Secondly, in addition to rotating a beam in one arm by α , a constant phase $\Delta\phi_c$ is added transforming D into

$$D' = \frac{1}{\sqrt{2}} \left(f(r)e^{i(4k+1)(\varphi+\alpha)+i\Delta\phi_c} - g(r)e^{i(4l+3)(\varphi+\alpha)+i\Delta\phi_c} \right). \quad (2.10)$$

As is indicated in the Fig.2.4, the angle of rotation α mimics the angles from the OAM sorter (in the opposite order) and needs to be set to $\alpha = \pi/2$. With these changes, correct destructive interference is observed in the channel F and constructive in E ,

$$\begin{aligned} E &= \frac{1}{2} \left(f(r)e^{i(4k+1)(\varphi+\pi/2)-i\pi/2} - g(r)e^{i(4k+3)(\varphi+\pi/2)-i\pi/2} + f(r)e^{i(4k+1)\varphi} + g(r)e^{i(4k+3)\varphi} \right) \\ &= f(r)e^{i(4k+1)\varphi} + g(r)e^{i(4l+3)\varphi}. \end{aligned} \quad (2.11)$$

In conclusion, the combiner on the right side takes in 4 inputs and generates a single beam in the output channel representing correctly swapped bit string.

Both versions of the swap operation transform the bits equally and the only difference is in their experimental implementation. Depending on our technical capabilities, we may prefer one over the other. Efficiency of the individual components is briefly discussed in the last chapter.

2.4 Operator notation of optical setups

With the increasing number of bits, the optical devices become more complicated and the diagrams less comprehensible. It might be advantageous to introduce a notation which simplifies the description of optical setups and expresses their full composition in a shortened form. Our proposed idea is in no sense a rigorous mathematical tool, it only provides instructions how to chain several simpler components in succession to manipulate a bit string in a desired way.

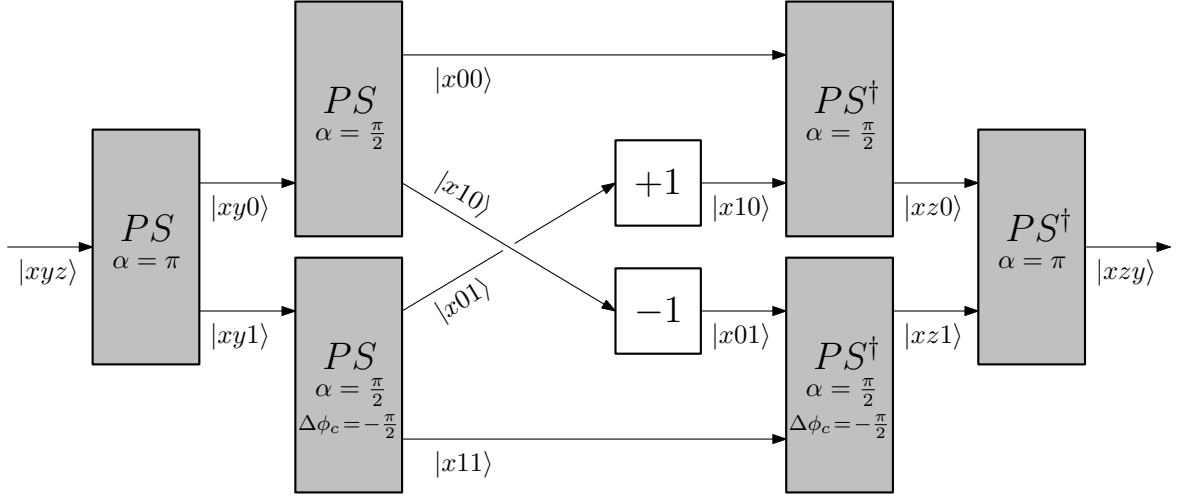


Figure 2.4: Improved device to swap last two bits. In contrast to the design in Fig.2.3 (which contains phase modulators $\times 2$ and $/2$), this one consists only out of 6 interferometers (3 normal and 3 inverted parity sorters) plus two holograms.

The notation is inspired by the scattering matrix formalism of optical systems and shares with it one key feature, linearity. The operators represent the building block of the diagrams like Fig.2.4. The domain and the range of our operators are bit strings. When there are multiple optical channels above one another depicted in the figure, we separate them with the symbol \oplus . This suggests that each operator may take one or multiple strings for input and produce one or multiple strings as an output. Chaining operators in a sequence will be expressed as a multiplication symbolized by a dot, $A \cdot B$. In contrast with the normal operator composition, the order in our notation is reversed, i.e. $(A \cdot B) |x\rangle = B(A(|x\rangle))$. The main reason for this little complication is that the dot notation better resembles the flow of time (from left to right) in the diagrams described by our equations.

The most basic component is the parity sorter, denoted as the operator $PS_{\alpha, -\Delta\phi_c}$. The lower index corresponds to the angle of rotation and the possible phase shift, as described in the previous sections. The domain of the $PS_{\alpha, -\Delta\phi_c}$ is one bit string, which is separated in two. For example, the operator PS_{π} takes $|xyz\rangle$ as an input and produces two bit strings (in two channels) expressed as $|xy0\rangle \oplus |xy1\rangle$. Usually, one parity sorter is followed by more, as in Fig.2.4, where the first two stages could be written as $PS_{\pi} \cdot (PS_{\pi/2} \oplus PS_{\pi/2, \pi/2})$. The inverted parity sorter is denoted by $PS_{\alpha, -\Delta\phi_c}^{\dagger}$.

The next key operator switches the positions of channels. We introduce the symbol $T_{(\cdot)}$, where the lower index is a cycle (or multiple cycles) denoting permutations of channels. (T stands for transposition, since P for permutation could be confused with the parity sorter PS .) The channels are numbered from the top and the total amount of them (permuted or not) is implied by the preceding operators. Note that the maximal length of the cycles will always be 2, since we only permute pairs of bit strings.

Switching of two channels is often followed by correction with a $\pm\delta$ -hologram adding a constant to OAM. This can be performed with a single string operator $F_{\pm\delta}$ signifying the value of the filter. The example in Fig.2.4 elucidates the use of T and F . The switch of the two middle channels together with the consequent OAM correction is expressed in our notation as $T_{(23)} \cdot (I \oplus F_{+1} \oplus F_{-1} \oplus I)$, where I is the identity, meaning nothing happens with that channel.

(Similarly $F_{\times 2}$ and $F_{/2}$ will denote some form of $\times 2$ - and $/2$ -modulation.)

The right and left shift are the last elementary operators for our toolbox. Instead of describing all the individual parts (± 1 , $/2$ and $\times 2$ modulators plus parity sorters), we simply denote them as R and L , abstracting from their inner structure. The right shift R takes one bit string $|xyz\rangle$ as an input and produces two outputs $|xy\rangle_0 \oplus |xy\rangle_1$. Conversely, the left shift L has two inputs and one output, where the order of the inputs is relevant. A demonstration of chaining several shifter operators is nicely seen in Fig.2.3. The whole diagram could be written symbolically

$$S_{12} = R \cdot (R \oplus R) \cdot T_{(23)} \cdot (L \oplus L) \cdot L. \quad (2.12)$$

The notation for the swap operator S_{12} includes the position of bits, which are being swapped when counting from the end. The order of the indices is unimportant (i.e. $S_{12} = S_{21}$), but the fact that we are counting bits from the right is, especially if used on larger bit strings ($S_{12} |xyz\rangle = |xzy\rangle$).

Of course, the same swap operation is illustrated in Fig.2.4. The ‘‘improved’’ version is given in the operator notation by

$$S_{12} = PS_{\pi} \cdot (PS_{\pi/2} \oplus PS_{\pi/2, \pi/2}) \cdot T_{(23)} \cdot (I \oplus F_{+1} \oplus F_{-1} \oplus I) \cdot (PS_{\pi/2}^{\dagger} \oplus PS_{\pi/2, \pi/2}^{\dagger}) \cdot PS_{\pi}^{\dagger}. \quad (2.13)$$

Since both implementations behave the same, the specific experimental construction is determined by the availability of the individual optical elements. The exact count is provided at the end of the section for both versions in Table 2.1, ‘‘ S_{12} with PS ’’ is given by the equation (2.13), and ‘‘ S_{12} with R, L ’’ by (2.12).

Another example might further illustrate our method. Take the swap operation of the first and third bit, $S_{13} |wxyz\rangle = |wzyx\rangle$. One implementation could be

$$\begin{aligned} S_{13} = & PS_{\pi} \cdot (PS_{\pi/2} \oplus PS_{\pi/2, \pi/2}) \cdot (PS_{\pi/4} \oplus PS_{\pi/4, 2\pi/4} \oplus PS_{\pi/4, \pi/4} \oplus PS_{\pi/4, 3\pi/4}) \cdot \\ & \cdot T_{(25)(47)} \cdot (I \oplus F_{+3} \oplus I \oplus F_{+3} \oplus F_{-3} \oplus I \oplus F_{-3} \oplus I) \cdot \\ & \cdot (PS_{\pi/4}^{\dagger} \oplus PS_{\pi/4, 2\pi/4}^{\dagger} \oplus PS_{\pi/4, \pi/4}^{\dagger} \oplus PS_{\pi/4, 3\pi/4}^{\dagger}) \cdot (PS_{\pi/2}^{\dagger} \oplus PS_{\pi/2, \pi/2}^{\dagger}) \cdot PS_{\pi}^{\dagger}. \end{aligned} \quad (2.14)$$

The first row describes the 3 stages of the OAM sorter in Fig.1.15, and likewise the last row is its inversion. The only interesting part is the middle row, which encodes switching two pairs of channels (2nd with 5th, and 4th with 7th) accompanied by ± 3 OAM modulators.

Whether the tuning of 8 optical channels proves to be too difficult, or the inefficiency of the ± 3 modulators introduces unbearable errors, there exists an alternative design for the S_{13} swap operator expressed as

$$S_{13} = S_{12} \cdot R \cdot (S_{12} \oplus S_{12}) \cdot L \cdot S_{12}. \quad (2.15)$$

The equivalence of both versions can be verified on a test bit string $|wxyz\rangle$ with a simple computation (where the operator compositions are applied from left to right)

$$\begin{aligned} S_{13} |wxyz\rangle &= (S_{12} \cdot R \cdot (S_{12} \oplus S_{12}) \cdot L \cdot S_{12}) |wxyz\rangle \\ &= (R \cdot (S_{12} \oplus S_{12}) \cdot L \cdot S_{12}) |wxyz\rangle \\ &= ((S_{12} \oplus S_{12}) \cdot L \cdot S_{12}) (|wxz\rangle_0 \oplus |wxz\rangle_1) \\ &= (L \cdot S_{12}) (|wzx\rangle_0 \oplus |wzx\rangle_1) \\ &= S_{12} |wzxy\rangle \\ &= |wzyx\rangle. \end{aligned} \quad (2.16)$$

To decide which realization of S_{13} is more suitable for our experiment, we tallied up the individual components in Table 2.1. Each row describes one of the previously discussed operations with their respective versions. S_{13} is mentioned three times, because there are two possibilities for the S_{12} swap in the alternative design (2.15). The second column “MZI” contains the total number of Mach-Zehnder interferometers, or equivalently, the number of parity sorters (since each PS is made out of one MZI). The symbol “ $\pm l$ ” indicates the number of filters raising or lowering OAM. Conversely, the next column labelled “max. l ” informs about the largest difference of OAM any filter may cause. “ $\times 2, /2$ ” stands for the number of modulators either doubling or halving the OAM. Only right and left shifters use them, and therefore any operation without R, L contains 0 $\times 2, /2$ -modulators. The last column reports on the maximum number of separate channels the operation will need at some point in the experiment.

The information in the table is calculated directly from the number of operators in the equations describing the given device. Take the entry “ S_{13} with S_{12} (with R, L)”, for which we compose the equations (2.15) and (2.12). The result tells us that there are $4 \times 6 + 2 = 26$ shifters (R and L), and 4 transposition operators $T_{(\cdot)}$. Every shifter comprises 1 interferometer, 1 filter with value ± 1 , and a pair of $/2$ -modulators (respectively $\times 2$ -modulators). The $T_{(\cdot)}$ does not change OAM and contains no filters. Hence, the number of every component in a shifter is multiplied by 26 to get the total amount. Finally, the maximum of separate channels can be, again, deduced from the equation (2.15). The part $(S_{12} \otimes S_{12})$ instructs to perform two S_{12} swaps in parallel, each requiring 4 separate channels. For this reason, our experiment needs to accommodate 8 optical channels next to each other.

	MZI	$\pm l$	max. l	$\times 2, /2$	max. channels
R resp. L	1	1	± 1	2	2
S_{12} with PS	6	2	± 1	0	4
S_{12} with R, L	6	6	± 1	12	4
S_{13} with PS	14	4	± 3	0	8
S_{13} with S_{12} (with R, L)	26	26	± 1	52	8
S_{13} with S_{12} (with PS)	26	10	± 1	0	8

Table 2.1: Table showing the constitution of different operations. “MZI” is the number of Mach-Zehnder interferometers. “ $\pm l$ ” represents the number of phase filters raising or lowering the OAM, whereas “max. l ” stands for the highest value from the phase filters. “ $\times 2, /2$ ” is the number of modulators, and finally “max. channels” states the maximum number of parallel channels required at some point in the operation.

Chapter 3

Quantum logic operations with OAM

A natural progression from the classical computation is to venture into the quantum domain. In the first section we present the concept of qubits and how to manipulate the quantum information with logical gates. Then follows a brief introduction to possible qubit realizations in physical systems with a focus on the optical alternatives. The third section contains a comprehensive description of optical gates we designed for qubits on OAM superpositions. Finally, the fourth section reviews some details needed to perform an experiment with the OAM qubits, in particular state preparation and measurement methods.

3.1 Qubits and quantum gates

Qubit is a quantum analogue to the classical bit, a unit characterizing an amount of information. Instead of having only two possible states, 0 or 1, a qubit can be in any normalized state from a complex two-dimensional Hilbert space spanned by vectors $|0\rangle$ and $|1\rangle$. These vectors are called computational basis states and their linear combinations are states $|\psi\rangle \in \mathbb{C}^2$ in the form

$$|\psi\rangle = \alpha |0\rangle + \beta |1\rangle, \quad (3.1)$$

where α, β are complex numbers satisfying the normalization condition $|\alpha|^2 + |\beta|^2 = 1$ [29, p. 13].

Similarly, a state of multiple qubits, say n , is a normalized vector from a Hilbert space $(\mathbb{C}^2)^{\otimes n}$, which has its computational basis denoted as

$$\begin{aligned} |0\rangle \otimes \cdots \otimes |0\rangle \otimes |0\rangle &= |0 \dots 00\rangle \\ |0\rangle \otimes \cdots \otimes |0\rangle \otimes |1\rangle &= |0 \dots 01\rangle \\ &\text{etc.} \end{aligned} \quad (3.2)$$

The number of basis vectors is, by definition, the dimension of the Hilbert space, which in this case is equal to 2^n . For example, a general state of a two qubit system can be expressed as

$$|\psi\rangle = \alpha |00\rangle + \beta |01\rangle + \gamma |10\rangle + \delta |11\rangle, \quad (3.3)$$

a normalized vector in \mathbb{C}^4 .

Manipulation of the quantum information stored by qubits is achieved by applying quantum gates to them. To be more precise, a physical change of a system is mathematically expressed by a unitary operator linearly acting on the state function of the system. The most essential

are operations on a single qubit represented by 2×2 unitary matrices. A few notable examples, written in the computational basis, are the gates

$$X = \begin{pmatrix} 0 & 1 \\ 1 & 0 \end{pmatrix}, \quad Y = \begin{pmatrix} 0 & -i \\ i & 0 \end{pmatrix} \quad \text{and} \quad Z = \begin{pmatrix} 1 & 0 \\ 0 & -1 \end{pmatrix}, \quad (3.4)$$

corresponding to the Pauli matrices σ_x , σ_y and σ_z , respectively. Also often encountered are the phase gate S and its square root $T^2 = S$ called $\pi/8$ -gate

$$S = \begin{pmatrix} 1 & 0 \\ 0 & i \end{pmatrix}, \quad T = \begin{pmatrix} 1 & 0 \\ 0 & e^{i\pi/4} \end{pmatrix}. \quad (3.5)$$

Note that the phase S is the square root of the Z gate, i.e. $S^2 = Z$. The final important example we mention here is the Hadamard gate

$$H = \frac{1}{\sqrt{2}} \begin{pmatrix} 1 & 1 \\ 1 & -1 \end{pmatrix}. \quad (3.6)$$

The previous gates are either diagonal, and only multiply the basis vectors by a constant, or are non-diagonal and only switch the position of the kets $|0\rangle$ and $|1\rangle$ with a possible multiplication by an imaginary unit. However, the H gate mixes both states equally and therefore it will be helpful to investigate its effect on a general state. The vector $|\psi\rangle$ defined in (3.1) is transformed by H into

$$H|\psi\rangle = \frac{\alpha + \beta}{\sqrt{2}}|0\rangle + \frac{\alpha - \beta}{\sqrt{2}}|1\rangle, \quad (3.7)$$

a result useful for a future section to design an optical equivalent of this gate.

Sometimes it is practical to think about quantum gates as rotations in the Bloch sphere, a representation of the qubit state space. The name rotational matrix is, however, reserved for exponentials of the Pauli matrices defined by

$$R_x(\theta) = \begin{pmatrix} \cos \frac{\theta}{2} & -i \sin \frac{\theta}{2} \\ -i \sin \frac{\theta}{2} & \cos \frac{\theta}{2} \end{pmatrix}, \quad R_y(\theta) = \begin{pmatrix} \cos \frac{\theta}{2} & -\sin \frac{\theta}{2} \\ \sin \frac{\theta}{2} & \cos \frac{\theta}{2} \end{pmatrix}, \quad R_z(\theta) = \begin{pmatrix} e^{-i\frac{\theta}{2}} & 0 \\ 0 & e^{i\frac{\theta}{2}} \end{pmatrix}. \quad (3.8)$$

They express rotations about the cardinal axes x, y, z , respectively, by an angle θ . Importantly, any unitary operation U on a single qubit can be decomposed into consecutive rotations and a phase factor [29, p. 175]

$$U = e^{i\alpha} R_z(\beta) R_y(\gamma) R_z(\delta). \quad (3.9)$$

Systems with multiple qubits can be manipulated with multi-qubit gates, which are again unitary matrices of the appropriate dimension. Note that single-qubit gates in larger systems are simply expressed as a tensor product of the two dimensional matrix with identity/identities, e.g.

$$I \otimes H \otimes I \quad (3.10)$$

means apply the Hadamard gate on the second qubit and leave the other two unchanged. On the other hand, actual multi-qubit quantum gates should affect more qubits and the information in one should influence the change of others. A primary and universal example is the controlled-NOT gate on two qubits. If the first qubit is labelled as control, when counting backwards, and the second indicates the target qubit, then applying the C_1NOT_2 gate to them switches the value of the target when the control is set to 1, in the computational basis. (The bit numbering

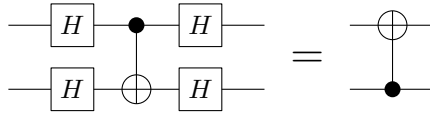


Figure 3.1: Quantum circuit diagram for decomposing the C_2NOT_1 into the set of universal gates.

from the right is in contrast with the standardized notation for the most and least significant bits. However, whether the value of OAM should be even or odd is decided by the last bit in its binary representation and manipulating the parity of OAM-beams is straightforward. Thus, for encoding quantum information into OAM, the last bit is the most easily accessible.) The matrix equivalent is given by

$$C_1NOT_2 = \begin{pmatrix} 1 & 0 & 0 & 0 \\ 0 & 0 & 0 & 1 \\ 0 & 0 & 1 & 0 \\ 0 & 1 & 0 & 0 \end{pmatrix}, \quad (3.11)$$

where the order of the vectors in the computational basis is $\{|00\rangle, |01\rangle, |10\rangle, |11\rangle\}$.

The universality mentioned earlier stands for the idea that an arbitrary quantum gate (on any number of qubits) can be decomposed into single qubit gates and the $CNOT$ [29, p. 191]. Thanks to the equation (3.9), one can further express the single qubit gates as Pauli rotations only. Therefore, when we design optical gates for OAM qubits in Section 3.3, it is sufficient to create single qubit rotations and the $CNOT$ operation between any pair of qubits. The other basic gates like X, Y, Z, H, S, T are implemented mainly for convenience, because they are very common.

The possibility to compose gates is very useful in general and can be used to create other gates not only in the context of the universality theorem. For example, take the standard C_1NOT_2 , where the value of the first qubit determines the action on the second (again, counting from the right). To reverse the role of the qubits, one can surround the C_1NOT_2 in the Hadamard gates, as shown in the quantum diagram Fig.3.1. Each horizontal wire denotes one qubit (first wire is the first qubit) and the order of application is from left to right. The box with one wire going in and one out represents a single-qubit gate, while the connection between the two parallel wires depicts a 2-qubit gate. In this instance, the black dot is the control qubit regulating the NOT -gate, the large plus sign in a circle. A little exercise in matrix manipulation reveals that the equation

$$(H \otimes H)C_1NOT_2(H \otimes H) = \begin{pmatrix} 1 & 0 & 0 & 0 \\ 0 & 1 & 0 & 0 \\ 0 & 0 & 0 & 1 \\ 0 & 0 & 1 & 0 \end{pmatrix} = C_2NOT_1 \quad (3.12)$$

is indeed satisfied.

3.2 Optical qubits on OAM superpositions

A qubit can be realized by various two level physical systems [29, p. 277], for example as trapped ions [30], nuclear spins in nuclear magnetic resonance [31], transmons in a superconducting solid [32], and most importantly for our purposes as degrees of freedom of a photon ranging from time and position to both angular momenta. Given the nature of our work, this section will

focus only on linear optical systems. Admittedly, nonlinear effects can mediate photon interactions in some implementations of *CNOT* gates for multi-photon qubits [33], but, in our study of OAM, common linear elements will suffice.

Photon spatial modes naturally exhibit quantum traits suitable for qubit implementation. The so-called dual-rail logic is defined as follows: the qubit is in the state $|0\rangle$ if the photon is travelling along the first path, and in $|1\rangle$ if the photon chose the second path [33]. Manipulation with the qubit can be handled entirely by beams splitters and phase shifters [34, 35]. Since the original references talk about beam splitters with variable reflectivity, in contrast to the fair ones used throughout this work, we imitate the different phases and reflectivity indices by an interferometric setup using adaptation of the idea from [29, p. 293] and [36]. As a demonstration, the Fig.3.2 shows implementation of the two non-diagonal rotational matrices R_x and R_y (defined by (3.8)) in Mach-Zehnder interferometer with extra phase filters. Moreover, it is possible to realize any discrete unitary operator on a N -state system efficiently in the number of required elements equal to $N(N - 1)/2$ [36].

An impractical trait of the spatial approach is its non-scalability. The reason is that, with the increasing number of qubits, the amount of optical paths increases exponentially [33]. The problematic growth in number of channels can be somewhat relaxed by employing more degrees of freedom of single photons. For example, a dual-rail photon with linear polarization can carry two quanta of information, one qubit in its position and the other in the orientation of its polarization [37]. Any single-qubit operation for polarization can be implemented with half- and quarter-wave plates, and transformation between both information carriers is facilitated by polarization beam splitters [33].

Another degree of freedom is the photons orbital angular momentum. Implementation of the OAM qubits is straightforward, since the previous chapters already prepared the ground theoretically and practically. LG modes form an orthonormal basis of paraxial beams and thus could naturally serve as computational basis states. Focusing only on the azimuthal index, the logical $|0\rangle$ can be represented as LG_0^0 , while the state $|1\rangle$ as LG_0^1 . Moreover, because the integer l is unbounded, multi-qubit states can be simulated similarly. A state of n qubits is a vector in 2^n -dimensional space and its basis can be formed by our LG_0^l modes. In fact, this representation immediately emerges by expressing l in base 2, for example the set

$$\begin{array}{cccccc}
 LG_0^0 & LG_0^1 & \dots & LG_0^6 & LG_0^7 & \\
 \updownarrow & \updownarrow & & \updownarrow & \updownarrow & \\
 |000\rangle & |001\rangle & \dots & |110\rangle & |111\rangle &
 \end{array} \tag{3.13}$$

could be the basis of a 3 qubit system, where the last binary digit is thought of as the first qubit, the next to last digit is the second qubit and so on. As was discussed before, the order of qubits is chosen from right to left, because the parity of l plays the most significant role in OAM manipulation.

The almost effortless polarization gates were a tempting alternative in our search for quantum OAM gates. Connection of the momenta can be achieved either by a modified parity sorter (with polarization beam splitters) [8] or through q-plates [9]. Nonetheless, we chose not to adopt polarization, since we already rely heavily on the OAM-position conversion, and inclusion of additional degrees of freedom would only complicate our designs. Section 3.3 presents optical elements we designed for OAM qubits.

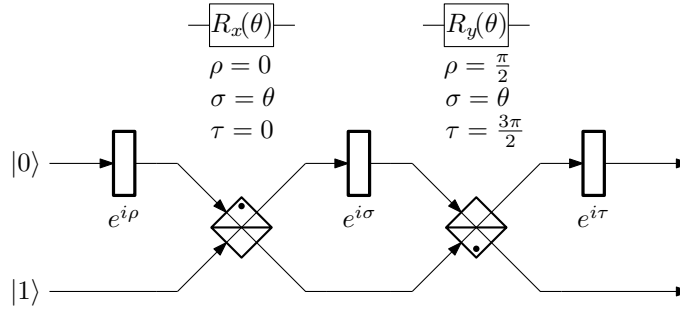


Figure 3.2: Optical realization of the rotational matrices for spatial qubits.

A note should be made on the recent efforts to use OAM as d -dimensional qubits (for $d > 2$), the so-called qudits [10]. The search for universal single-qudit gates progressed with successful experiments in 4 dimensions [23, 38], and was followed by extensive theoretical work on these Pauli operators in arbitrary dimension [27, 28]. However, given the binary decomposition of OAM in our approach, the cyclic permutation operators (generalized X gates) are not very suitable. Instead of increasing the whole register by 1, we decided to control the position of individual bits by shifters and swaps prepared in Chapter 2.

3.3 Optical gates for OAM qubits

Since superpositions of the OAM states of a beam can be perceived as states of a system of qubits, it would be convenient to possess some means to manipulate them. Fortunately, the bulk of the work has already been done in Chapter 2 where we discussed classical logical operations. All of the devices there were designed with superpositions of OAM in mind and therefore adaptation for the quantum computations is straightforward. The most utilized instrument will be the parity sorter with its counterpart, the inverted parity sorter, which allow us to separate a desirable bit and transform its information into position. First, we consider gates only on the first qubits (or pairs of qubits), and then provide a solution for an arbitrary position of the manipulated qubit at the end of the section.

Diagonal single-qubit gates, namely the Z gate, the phase S and the T gate, do not permute or combine the basis vectors and only multiply them by a constant. As was mentioned before, a simple parity sorter can distinguish between beams with even and odd values of OAM, that is whether the last bit in the binary string is 0 or 1. Focusing for now only on the first qubit, any beam in superposition defined by (3.1) is separated by the parity sorter with $\alpha = \pi$ into two arms, as is illustrated in Fig.3.3. Each individual beam can then go through its own phase plate to introduce a different phase delay to both basis vectors. Lastly, the inverted parity sorter recombines both beams into one output, creating the desired state. To simulate the effect of the diagonal gates from the first section, only one phase plate is needed. The Z gate is produced by the delay $e^{i\pi} = -1$ in the bottom arm corresponding to the ket $|1\rangle$. Likewise, the phase and the $\pi/8$ gate are created with the phase plates $e^{i\pi/2}$ and $e^{i\pi/4}$, respectively. Admittedly, two phase plates can be installed in the device, one in each arm, to build any diagonal gate, e.g. R_z .

On the other hand, the X and Y gates not only multiply the vectors by a constant, but also permute their order. A general scheme for any non-diagonal gate is presented in Fig.3.4 with two phase plates and two modulators adding or subtracting the OAM. Actually, only the modulators

carry out the swap of the basis vectors $|0\rangle \leftrightarrow |1\rangle$ and for the X gate no phase plates are even necessary. Y is achieved by including the appropriate phase delay in each arm, as suggested in the Fig.3.4.

The next single-qubit operation from our list in Section 3.1 is the Hadamard gate. The idea for its implementation comes from the realization that the Hadamard matrix is exactly the same as a matrix of a 50/50 beam splitter [37]. As in the previous cases, we begin by transforming the OAM into a spatial qubit. Before combining both beams, they need to have the same OAM, and therefore we send one through a ± 1 filter. We chose to decrease the OAM of the bottom beam and make both even in the illustration Fig.3.5. When operating with a beam splitter, it is important to keep in mind the asymmetry of its outputs. The dot in our figures signifies the output in which the difference applies. Although the orientation in Fig.3.5 produces correctly the sum in the top output, the remainder after subtracting in the bottom has the opposite sign to what the H matrix predicts. For this reason, the $e^{i\pi}$ filter along with the $+1$ hologram are included in the lower arm before recombining. (Another solution would be to rotate the beam splitter 180° and swap the outputs.)

To conclude the overview of OAM single-qubit operations, the rotations R_x and R_y can be performed by the setup in Fig.3.2, which again would be placed between a set of parity sorters (and ± 1 filters). Ultimately, a series of these rotational operations can create any unitary gate with the composition given by the equation (3.8).

Thanks to the universality theorem, the only multi-qubit gate we need to be able to construct on OAM superpositions is the $CNOT$. Considering the discussion about the C_1NOT_2 matrix (3.11) and how it transforms the basis vectors, we designed the optical setup in Fig.3.6, which performs the proper operation. The whole diagram can be expressed in our symbolic operator notation of Section 2.4 as

$$C_1NOT_2 = PS_\pi \cdot (I \oplus PS_{\pi/2, \pi/2}) \cdot T_{(23)} \cdot (I \oplus F_{-2} \oplus F_{+2}) \cdot (I \oplus PS_{\pi/2, \pi/2}^\dagger) \cdot PS_\pi^\dagger. \quad (3.14)$$

An incomplete two-stage parity sorter separates the superposition of two qubits (3.3) into three channels (the full two stage sorter is not necessary, since nothing happens to the even-valued vectors), after which the two channels transmitting the states with the control qubit equal to 1, and the target equal to 0 and 1 exchange positions, i.e. $|01\rangle \leftrightarrow |11\rangle$. To merge all channels back, the OAM of the switched states needs to be first corrected by a couple of ± 2 modulators before going through the inverted parity sorters. The output of the setup is equivalent to transforming the vector $|\psi\rangle$ from (3.3) by the C_1NOT_2 matrix (3.11).

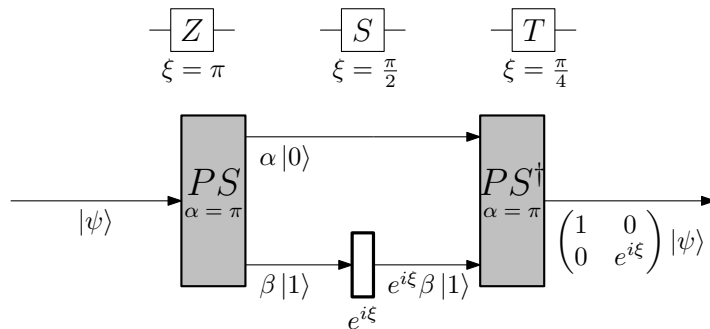


Figure 3.3: Optical realization of the diagonal single-qubit gates.

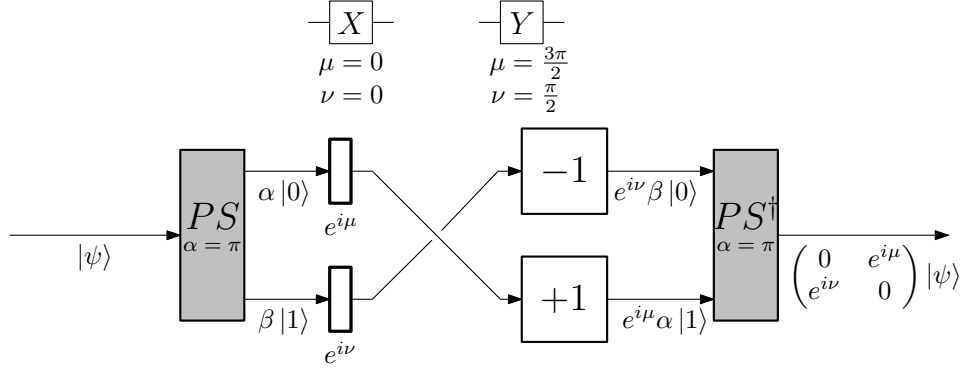


Figure 3.4: Optical realization of the non-diagonal single-qubit gates.

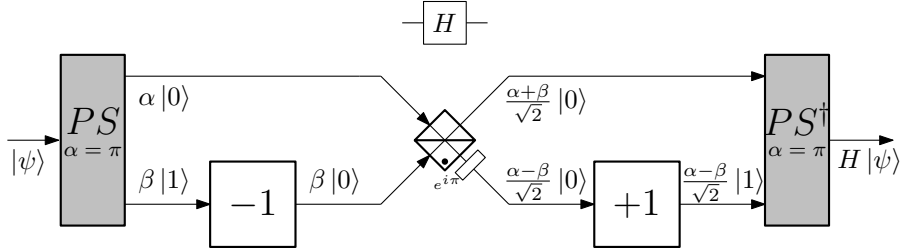


Figure 3.5: Optical realization of the Hadamard gate.

Other combinations of the control and target qubit (which two qubits the $CNOT$ should affect) are implemented straightforwardly. To construct the reverse C_2NOT_1 gate, instead of chaining four versions of the Hadamard gate designed in Fig.3.5 and one C_1NOT_2 as was discussed in the equation (3.12) and Fig.3.1, one can simply adapt the idea from the earlier C_1NOT_2 . The reverse operation has the control qubit in the second position, and therefore we need to switch the channels with 1 as the second digit in the binary OAM representation. The whole setup is described by the equation

$$C_2NOT_1 = PS_\pi \cdot (PS_{\pi/2} \oplus PS_{\pi/2, \pi/2}) \cdot T_{(23)} \cdot (I \oplus F_{-1} \oplus I \oplus F_{+1}) \cdot (PS_{\pi/2}^\dagger \oplus PS_{\pi/2, \pi/2}^\dagger) \cdot PS_\pi^\dagger \quad (3.15)$$

and illustrated in Fig.3.7 along with the necessary ± 1 modulators. Alternatively, the swap operation S_{12} from the Section 2.3 could be used to change the position of the target and control, then apply the regular C_1NOT_2 , and finally return the bits to their original position. Thus, surrounding the gate with two S_{12} operators in our notation

$$C_2NOT_1 = S_{12} \cdot C_1NOT_2 \cdot S_{12}, \quad (3.16)$$

would achieve the objective. Comparison of both version in terms in term of required elements is provided in Table 3.1 and further discussed in Chapter 4.

So far, all the optical gates were designed only for the first qubit or a pair of qubits (i.e. the last digit in its bit string representation). Thankfully, Chapter 2 provides a solution to reach qubits in other positions. For the single-qubit gates, an immediate idea is to use the right shifter several times to get the qubit to be transformed (say in a position n from the end) to the first place (rightmost). However, each right shifter creates two optical paths (carrying information

about the lost qubit), both of which have the targeted qubit in the $(n - 1)$ -th position. Further shifting sends the qubit closer to the first position for the price of increase in the number of channels. After $n - 1$ stages of right shifting, on one hand, we have the targeted qubit in correct place, but on the other hand, the qubit is divided into 2^{n-1} channels. And, accordingly, 2^{n-1} copies of the chosen gate are necessary to transform the qubit.

The exponential growth in the number of gates is a direct consequence of transforming the “lost” information (from the qubits to the right of the one being moved) into position. To avoid this problem one can use a generalization of the swap operation from the Section 2.4. Take, for example, the third qubit from the right that we want to transform with a quantum gate U . Either we use four copies of U as described above, or we take advantage of the swap S_{13} device and implement one gate U on its output. Disadvantage of the swap method is the increased number of shifters, because two swaps are always needed (forward and back), and the larger distance between swapped qubits, the more complicated the operation becomes. For more details, see Chapter 4, since experimental realization of both possibilities will come down to the efficiency of all components and their complexity. Producing several copies of the Z gate (Fig.3.3) may be feasible, whereas aligning all the beam splitters in the R_x gate (Fig.3.2) might be challenging to replicate multiple times.

Similar options present themselves when designing the $CNOT$ gate for an arbitrary control and target qubit. A demonstration could be made with the C_1NOT_3 gate. The first possibility

$$C_1NOT_3 = S_{23} \cdot C_1NOT_2 \cdot S_{23} \quad (3.17)$$

uses some form of the S_{23} swap (for example $S_{23} = R \cdot (S_{12} \oplus S_{12}) \cdot L$). If this new swap operation is too difficult to implement, one could rely on the basic S_{12} and include more $CNOT$ gates, as in

$$C_1NOT_3 = S_{12} \cdot R \cdot (C_1NOT_2 \oplus C_1NOT_2) \cdot L \cdot S_{12}. \quad (3.18)$$

The final alternative

$$\begin{aligned} C_1NOT_3 = & PS_\pi \cdot (I \oplus PS_{\pi/2, \pi/2}) \cdot (I \oplus PS_{\pi/4, \pi/4} \oplus PS_{\pi/4, 3\pi/4}) \cdot \\ & \cdot T_{(23)(45)} \cdot (I \oplus F_{-4} \oplus F_{+4} \oplus F_{-4} \oplus F_{+4}) \cdot \\ & \cdot (I \oplus PS_{\pi/4, \pi/4}^\dagger \oplus PS_{\pi/4, 3\pi/4}^\dagger) \cdot (I \oplus PS_{\pi/2, \pi/2}^\dagger) \cdot PS_\pi^\dagger \end{aligned} \quad (3.19)$$

comprises an incomplete three-stage OAM sorter, with two sets of ± 4 filters in the middle. All three solutions have their pros and cons, but the choice of a specific version could be based on the total number of optical elements. The data is provided in the Table 3.1, where the “ C_1NOT_3 with S_{23} ” gate uses the aforementioned $S_{23} = R \cdot (S_{12} \oplus S_{12}) \cdot L$ swap, and all the S_{12} swaps are “with PS ” given by (2.13). The simpler C_1NOT_2 and C_2NOT_1 are also included.

	MZI	$\pm l$	max. l	$\times 2, / 2$	max. channels
S_{23}	14	6	± 1	4	8
C_1NOT_2	4	2	± 2	0	3
C_2NOT_1	6	2	± 1	0	4
C_2NOT_1 with S_{12}	16	6	± 2	0	4
C_1NOT_3 with S_{23}	32	14	± 2	8	8
C_1NOT_3 with two C_1NOT_2	22	10	± 2	4	6
C_1NOT_3 with PS	8	4	± 4	0	5

Table 3.1: Table comparing the composition of the different $CNOT$ gates. The meaning of the labels above the columns is explained in the Table 2.1 and the preceding text.

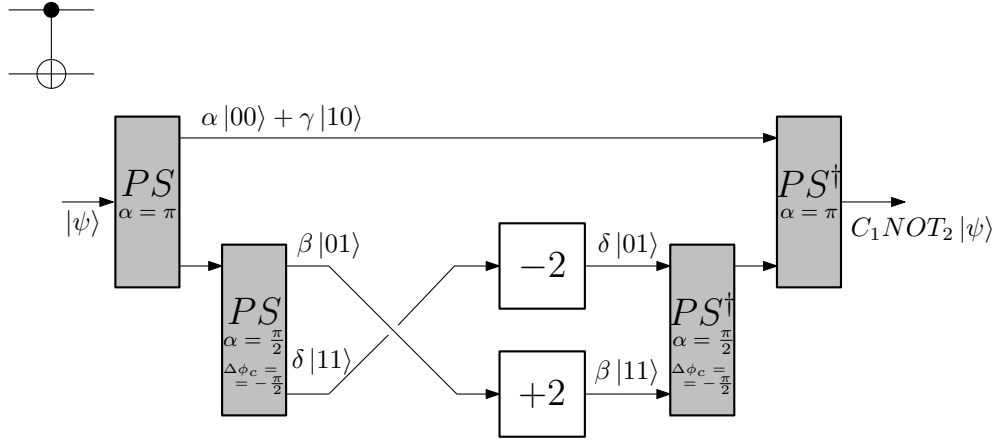


Figure 3.6: Optical realization of the C_1NOT_2 gate.

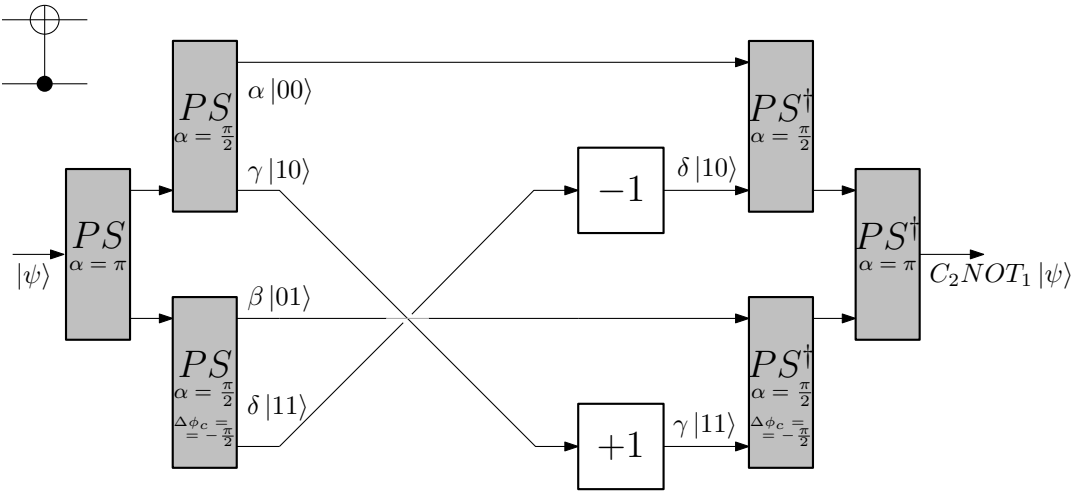


Figure 3.7: Optical realization of the C_2NOT_1 gate.

3.4 State preparation and measurement

A key requirement of every quantum computation is to have the desired input. Without the knowledge of the initial state in our experiment, we cannot conclude anything useful from the results. Moreover, the input needs to be prepared reliably multiple times in order to repeatedly run the computation. Generally, only the state $|0\dots 0\rangle$ is necessary to commence an experiment [29, p. 281], since the correct quantum operations can produce any other state. In other words, the first few gates in a quantum circuit serve as a state preparation before the actual computation.

The OAM qubit equivalent of the state $|0\dots 0\rangle$ is the mode LG_0^0 , i.e. a Gaussian beam. Preparation of a Gaussian beam with a conventional laser and lenses is straightforward and therefore easily repeatable. Subsequently, the input can be manipulated into any desired state by applying our OAM optical gates. However, due to the complexity of the designs, we may want to reduce the number of total gates as much as possible.

In some cases we might save on a few optical elements by remembering what our bit strings represent. For example, it is less challenging to generate a pure LG mode than to shift bits back and forth several times (and apply single-qubit gates) to create the corresponding pure state. One forked hologram with higher number of dislocations can substitute the function of dozens of parity sorters. On the other hand, mixed states cannot be similarly created without additional equipment. It is possible to combine two different LG modes on an inverted parity sorter, but only if their azimuthal numbers are in the correct congruence class (see Section 1.5). Mixing beams with their values l “far apart” (in the sense of the congruence) would require multiple stages of the inverted OAM sorter.

To read the result from a quantum computer, a measurement is needed to convert the quantum information into classical. Suppose a photon carries a superposition

$$|\psi\rangle = \sum_{x,y,z \in \{0,1\}} \alpha_{xyz} |xyz\rangle \quad (3.20)$$

of several qubits encoded in its OAM. According to the quantum postulate [29, p. 84], measurement of OAM in the computational basis of the qubits gives the result $l = (xyz)_2$ with the probability $|\alpha_{xyz}|^2$. Although our designs theoretically work on a photon-level, there is no reason to perform single photon experiments (because of the difficulties with generating/detecting single photons and inherent losses of the system) and it would be more practical to use full intensity beams. With beams, instead of counting detection events, we measure the intensities of individual OAM components, which are proportional to the probabilities $|\alpha_{xyz}|^2$.

OAM detection methods were already discussed in Section 1.5 and can be performed in two steps. First, an OAM separator (inverted OAM sorter in Fig.1.15) or another mode sorter transforms one beam into a superposition state of n qubits into 2^n beams in single LG modes. Second, CCD or an intensity detector measures the intensity of each output beam. As a confirmation of our experimental precision, the total intensity of the individual OAM components should be equal to the input intensity after subtracting the overall built-in losses of the experimental equipment.

Chapter 4

Realizability

With the set of universal OAM gates we are theoretically ready to build a simple linear-optical quantum computer and in this chapter we discuss the feasibility of such a task. Since $\times 2$ - and $/2$ -modulators were our main contribution in the first chapter, we begin by comparing the transformed beams with the targeted LG modes. The first two sections are concerned with method A and B, respectively, in which we numerically simulate how much intensity of the modulated beams is in the desired LG_0^{2l} and $LG_0^{l/2}$. In the third section the efficiency of $\pm\delta$ -holograms is discussed. In the last section all the results are put together and applied to our OAM quantum gates. The efficiency of the different operations is computed based on the throughput of the individual components.

4.1 $\times 2$ - and $/2$ -modulation with method A

The $\times 2$ - and $/2$ -modulators are key components in our shift operations and we are naturally interested if they function properly. Chapter 3 established that qubits will be represented as Laguerre-Gaussian beams carrying OAM and therefore the input of the modulators will be LG modes or their superpositions. In most instances the shifters are a part of a more complex system and hence the output of the modulators should resemble LG modes as well so that the consequent operations receive input in the correct form.

The realizability of both modulation methods, A and B, will be studied with LG_0^0, \dots, LG_0^7 beams only. The reason is mainly because these LG modes represent all states of 3 qubits. For 4 qubits, we would need LG modes up to $l = 15$.

First, let us compare the difference between $F_{\times 2}(LG_0^l)$ and LG_0^{2l} . Transformations of the six LG modes LG_0^1, \dots, LG_0^6 are simulated in the Fig.B.1 and Fig.B.2. (This selection was made on account of the size of our plots: modulation of LG_0^0 is not that interesting and LG_0^7 is similar to the other large l beams.) Output of the modulator is shown in the second column, where an unforeseen “triangular” deformation emerges. As the azimuthal number increases, the triangle becomes more apparent. Even though the result hardly looks like LG_0^{2l} , if one counts the number of times the phase changes when going around the periphery of the triangle shape, the total amount is indeed $2l$. (More about phase changes and singularities is discussed below.)

With the hopes of correcting the distortion, we let the output naturally evolve in space. The third column displays the modulator output after free space propagation over distance z_R . It can be clearly seen that the higher-order components expand rapidly and leave our sampling area. On the other hand, the propagation seems to smoothen the triangle deformation, to a certain

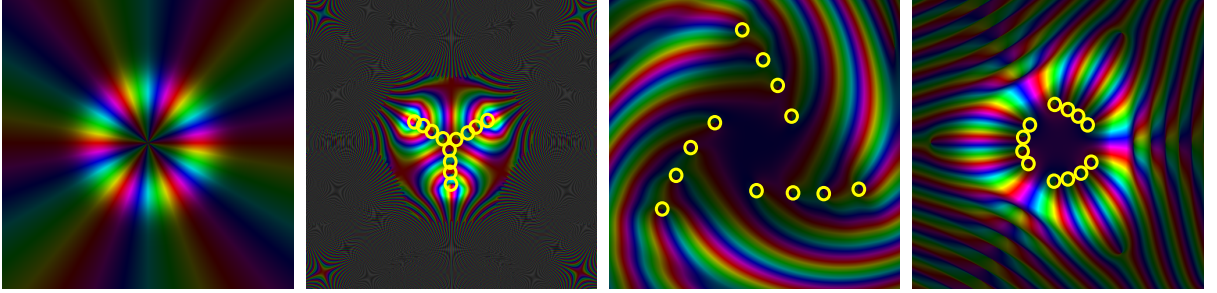


Figure 4.1: Phase profiles of LG_0^6 with highlighted singularities in different stages of modulation. The figures do not represent physical intensity distribution of the beams, since peripheries with no intensity are artificially brightened to show the complete phase distribution. From left to right: untransformed input beam, LG_0^6 right after $\times 2$ -modulation with method A, then propagated over z_R , and lastly transformed by a lens.

extent. We also tried to let the beam propagate to infinity by imaging the modulator output onto a Fourier plane of a lens with the focal length $f = 0.5 z_R$ (last column), which allows us to observe the beam’s angular distribution. Unfortunately, the triangle shape still remains in the Fourier image, but at least the phase variance is perceptibly distributed more evenly.

After a close inspection of the most misshaped profile, the $\times 2$ -modulated LG_0^6 , one can notice several phase singularities in the vertices of the “triangle”. A phase singularity is a point in the transverse plane of the beam around which the phase changes by 2π (or an integer multiple thereof) [6]. Investigating the behaviour of the singularities could reveal how closely the modulated beams resemble their untransformed counterpart LG_0^{2l} . Fig.4.1 illustrates the phase profiles of the beams LG_0^6 and its transformations in the same order as in the Fig.B.1. Each plot is superimposed with a plot showing purely the phase profile, lowering the contrast in the dark regions. For convenience, the singularities are marked with a yellow circle. The original LG_0^6 has one singularity of order 6 in the center (not highlighted), whereas the transformed beams have $6 \times 2 = 12$ first-order singularities of the first order distributed within the bright ring (on the inside of triangle). (Notice there are many more singularities outside the “triangle area”, but the intensity at those points is basically zero and thus they can be ignored as noise.) Although a positive result could be that the total charge, i.e. the total number and headedness, of the singularities is conserved, the targeted pure mode LG_0^{12} , which we wanted to create, has only one singularity of order 12 in the center.

Alternatively, we could look at Fourier coefficients to quantify the overlap of our transformed beams with the standard LG modes. The idea is based on the fact that LG modes form a complete orthonormal basis and any paraxial beam can be expressed as

$$|\psi\rangle = \sum_{p \in \mathbb{N}_0, l \in \mathbb{Z}} \alpha_{p,l} LG_p^l, \quad (4.1)$$

where the complex numbers $\alpha_{p,l}$ are the Fourier coefficients $\alpha_{p,l} = \langle p, l | \psi \rangle$.

The magnitudes of the coefficients $|\alpha_{p,l}|^2$ are plotted in Fig.4.2 for values $l \in \{0, \dots, 20\}$ and separately for $p \in \{0, 1, 2, 3\}$. The inputs $|\psi\rangle$ are the $\times 2$ -modulated modes LG_0^0, \dots, LG_0^7 transformed by the width-correcting lens, i.e. the last figures in the $\times 2$ rows in Fig.B.1 and

Fig.B.2. An immediate observation could be that the overlap with the targeted LG_0^{2l} modes is no more than 20% for any of the transformed beams except for the Gaussian $F_{\times 2}(LG_0^0)$. A lot of the remaining intensity can be found in modes with higher index p , in case of the first 4 beams $F_{\times 2}(LG_0^0), \dots, F_{\times 2}(LG_0^3)$, whereas the $F_{\times 2}(LG_0^4), \dots, F_{\times 2}(LG_0^7)$ are transformed into a combination of different LG_0^l modes. Interestingly, the maximum value of $|\alpha_{0,l}|^2$ for these higher order modes is not in the targeted LG_0^{2l} . For example, the beams $F_{\times 2}(LG_0^6)$ and $F_{\times 2}(LG_0^7)$ have almost negligible overlap with the LG_0^{12} and LG_0^{14} , respectively.

A possible explanation is following: first of all, the inner product greatly depends on the width of the two beams. The $\times 2$ -modulation changes not only the phase, but also the radial distances, which affects the size of the beams and consequently appears as overlap with higher- p modes. To a certain extent, we can mitigate the size change by a correct choice of the second lens, but no single focal length can rectify all beams. A second defect of the whole method is the impeding triangle deformation. Along the shape distortion, the phase also suffers an uneven distribution. This projects onto the coefficients $|\alpha_{0,l}|^2$, which have local maxima in points separated by multiples of 3. We point out an example $F_{\times 2}(LG_0^4)$: for $p = 0$ the significant (nonzero) values of $|\alpha_{p,l}|^2$ are in $l = 2, 5, 8, 11$ and 14 and similarly for $p = 1$ in $l = 8$ and $l = 11$.

In summary, the $\times 2$ -modulator in method A does not behave as we wanted. A significant problem seems to be in the width of the beams, which causes higher p modes to emerge. Moreover, the triangular deformation considerably affects beams with larger l . Combination of both of these defects results in beams $F_{\times 2}(LG_0^4), \dots, F_{\times 2}(LG_0^7)$ having the largest overlap not with LG_0^{2l} but instead with $LG_0^{2l\pm 3}$. The phase-amplitude hologram itself is also responsible for the loss of 50% intensity. The rest is distributed between different LG modes, which can be confirmed with the sum of all coefficients $|\alpha_{p,l}|^2$ for the individual beams shown in Table 4.1. The norm of the modulated beam and the wanted value $|\alpha_{0,2l}|^2$ are also included in the table. The difference between the first and second row can be probably found in the contributions from LG modes with $l > 20$, which we did not compute. We did, however, search for the missing intensity in negative l modes, but the only notable values were present in the $F_{\times 2}(LG_0^1)$ decomposition tallying up to 0.017. The higher-order modulated modes have the total overlap with the negative modes less than 1%.

Notice the norm of $F_{\times 2}(LG_0^0)$ is larger than the rest. The improvement in efficiency may be explained by the phase-amplitude modulator, which has real values ranging from -1 to 1 , and in the center of the modulator there is a region with only positive values. The narrow Gaussian beam entering the modulator is affected mostly by this region, while only a small part of the beams less intense periphery is modulated by the “negative” areas of the modulator. Thus if we compute the norm of the modulated LG_0^0 mode, the dominant central region will contribute the most. On the other hand, a general LG mode is shaped as a ring. When such a beam goes through the modulator, it encounters roughly the same number of the positive and negative regions. Therefore the square of the norm is taken as the average between 0 and 1.

$F_{\times 2}(\cdot) \parallel$	LG_0^0	LG_0^1	LG_0^2	LG_0^3	LG_0^4	LG_0^5	LG_0^6	LG_0^7
$\ \cdot\ ^2 =$	0.54	0.50	0.50	0.50	0.50	0.50	0.50	0.50
$\sum \alpha_{p,l} ^2 =$	0.53	0.47	0.49	0.49	0.48	0.48	0.44	0.42
$ \alpha_{0,2l} ^2 =$	0.21	0.18	0.16	0.12	0.07	0.03	0.03	0.01

Table 4.1: $\times 2$ -modulation with method A. The first row contains the square of the norm for the modulated beams $F_{\times 2}(LG_0^0), \dots, F_{\times 2}(LG_0^7)$. The second row tallies the coefficients from the plots in Fig.4.2, while the last row shows only the targeted value $|\alpha_{0,2l}|^2$.

The $/2$ -modulator of method A can be studied in a similar fashion. Figure B.1 plots the transformation of even-valued LG modes, where the second column shows the beams right after the modulator. The azimuthal phase gradient resembles $LG_0^{l/2}$ pretty convincingly, but an interference pattern disturbs the overall profile. Free space propagation, however, clears the irregularities and, based on the plots in third column, the modulated beam propagates like a proper LG mode. Following the same logic as the $\times 2$ -modulation, the last image in each row shows the output from the modulator displayed by a lens (with $f = 2.27 z_R$) proving that the angular distribution is indeed stable.

Fig.B.2 illustrates our attempt to divide odd- l beams by 2. The first plot shows asymmetrical phase distribution dimmed by interfering parts of the beam. Even after a short distance propagation, most of the intensity leaves the central part. Therefore some of the figures had to be artificially brightened to show anything at all. Ultimately, nothing reaches the second Fourier plane of the second lens, which we do not show, as it would be only a black square. These simulations confirm that dividing an odd OAM by 2 is not meaningful.

Comparison of our modulated beams with their targeted $LG_0^{l/2}$ is most easily seen on the Fourier coefficients. Calculated values of the $|\alpha_{p,l}|^2$ are plotted in Fig.4.3 for the even- l beams only. Since the modulation widens the beams, the inner products in equation (4.1) were computed for modulated beams transformed by an additional lens, which corrects their size to a certain extent, i.e. the last column in Fig.B.1. The focal length was chosen as $f = 2.27 z_R$ to maximize the overlap of the wider, higher l modes and hence it had adverse impact on the narrow LG_0^0 mode. Apart from the Gaussian beam, the rest of the $/2$ -modulated beams have over 40% of their intensity in the correct mode. The contribution from LG modes with higher p is almost negligible.

Overall the OAM division with method A behaves as expected and creates an output close the targeted $LG_0^{l/2}$. The downside is inefficiency of the phase-amplitude modulator, which introduces too many losses. Comparing the norm of the modulated beams and the total of the coefficients in Table 4.2, it is safe to assume that we calculated inner products with enough LG modes. There is only some missing intensity of the Gaussian beam, which may be found in higher p modes. Additional computations reveal overlap of $F_{/2}(LG_0^0)$ with LG_p^0 almost linearly decreasing in p , in which even $|\alpha_{10,0}|^2$ is still approximately 0.7%.

$F_{/2}(\cdot)$	LG_0^0	LG_0^2	LG_0^4	LG_0^6
$\ \cdot\ ^2 =$	0.54	0.48	0.47	0.43
$\sum \alpha_{p,l} ^2 =$	0.43	0.46	0.47	0.42
$ \alpha_{0,l/2} ^2 =$	0.29	0.40	0.44	0.41

Table 4.2: $/2$ -modulation with method A. The first row shows the norm for the modulated beams $F_{/2}(LG_0^0), \dots, F_{/2}(LG_0^6)$ with even l . In the second row is the sum of the coefficients from the plots in Fig.4.3, while the last row contains only the targeted value $|\alpha_{0,l/2}|^2$.

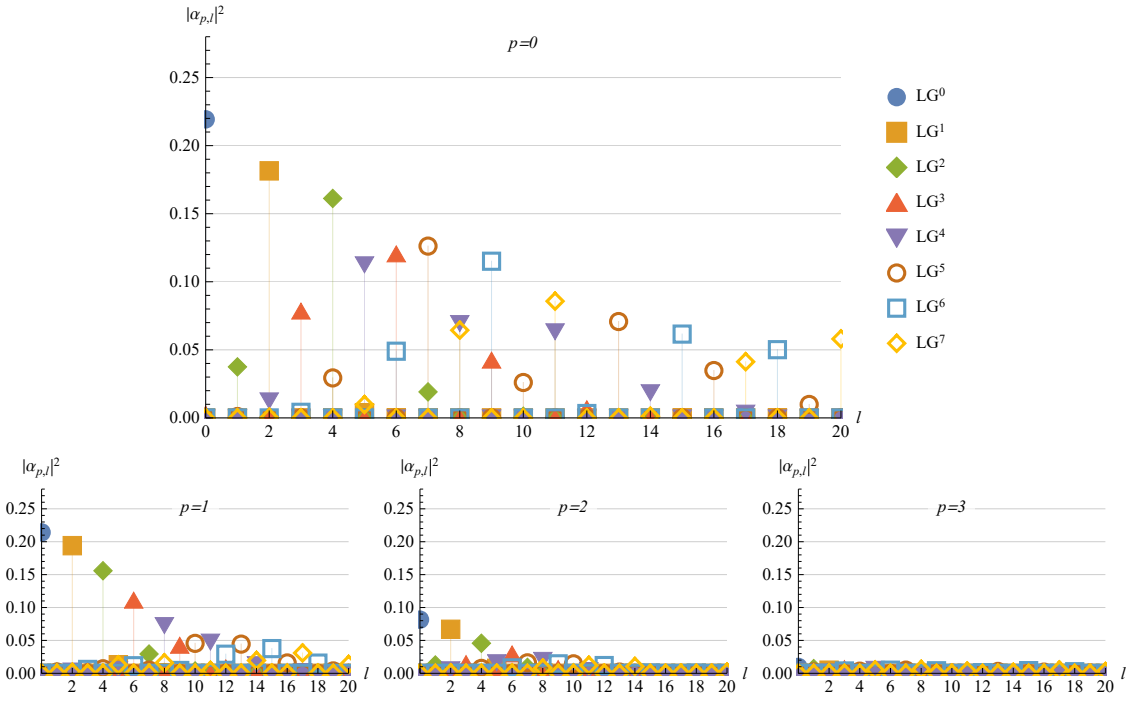


Figure 4.2: Method A: $F_{\times 2}(LG_0^l)$ beams after the width-correcting lens (i.e. the last column in Fig.B.1 and Fig.B.2) compared to standard LG_p^l modes.

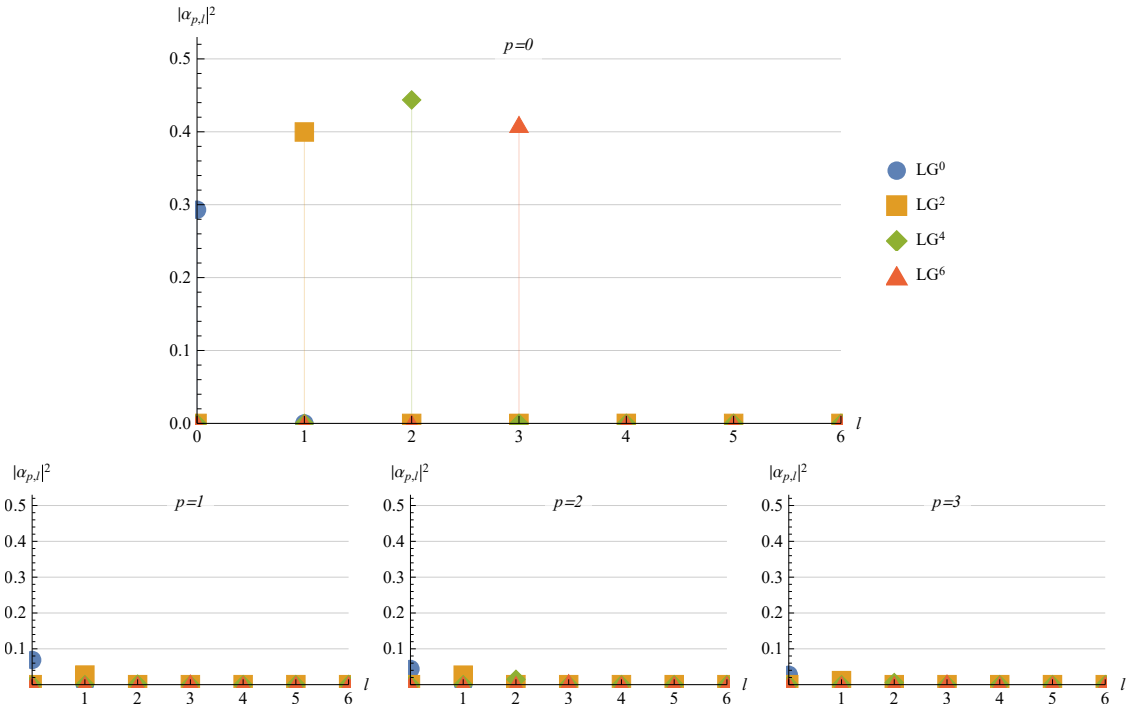


Figure 4.3: Method A: $F_{/2}(LG_0^l)$ beams after the width-correcting lens (i.e. the last column in Fig.B.1) compared to standard LG_p^l modes.

4.2 $\times 2$ - and $/2$ -modulation with method B

The optical setup in Fig.1.10 for method B was designed to avoid the inherent losses of the phase-amplitude modulators used in method A. For easier comparison of the differences, all plots in Fig.B.3 and Fig.B.4 are created with the same conditions and follow the same structure as in the case of method A (as well as the same lenses for $\times 2$ - and $/2$ -modulation, respectively).

$\times 2$ -modulation with method B faces even stronger deformations than method A. Due to the two mirrored input modulators (1.16), the two halves of the triangle formed in the output are oriented the opposite way and do not match with each other. It can be seen most clearly on the beam with the largest index l , $F_{\times 2}(LG_0^6)$, in which the two halves try to connect in different places. Additionally, some parts of the half-triangle leak from one half to the other, where they encounter modulator with the wrong phase correcting function. Although this creates small ripples along the vertical axis, a free space propagation quickly clears the imperfections, as seen in the third column of Fig.B.3 and Fig.B.4. The last columns of the figures plot the angular distribution of our transformed beams, in which the two halves are connected almost seamlessly and do not exhibit any of the aforementioned defects.

Similar improvement with propagation can be observed on the phase singularities. A great fault of the OAM multiplication with method B is that the triangle shape is sliced exactly through one of the vertices containing a third of the total singularities (see Fig.4.1). Joining the two halves together forms a whole line of phase discontinuity where many singularities develop, as shown in the second plot of Fig.4.4. In fact, there are so many positive (yellow) and negative (red) singularities along the vertical axis and especially in the center, that we were unable to highlight them all. Fortunately, according to the third image of Fig.4.4, letting the beam evolve in free space clears up the phase profile and most of the line discontinuities either leave the middle part or merge (positive and negative singularities cancel each other out). In this plot, the total charge of all the present singularities is $14 - 2 = 12$. Likewise, the last plot with Fourier image of the modulated beam has 12 singularities of the first order in the central area.

The constitution of our transformed beams can again be seen by decomposing it into the basis of LG modes. Values of the Fourier coefficients $|\alpha_{p,l}|^2$ are plotted in Fig.4.6 for the $\times 2$ -modulated beams after the width-correcting lens. A hindrance is, as always, the width of the beams, which results in large overlap with the higher p modes. The small l modes, $F_{\times 2}(LG_0^0), \dots, F_{\times 2}(LG_0^4)$,

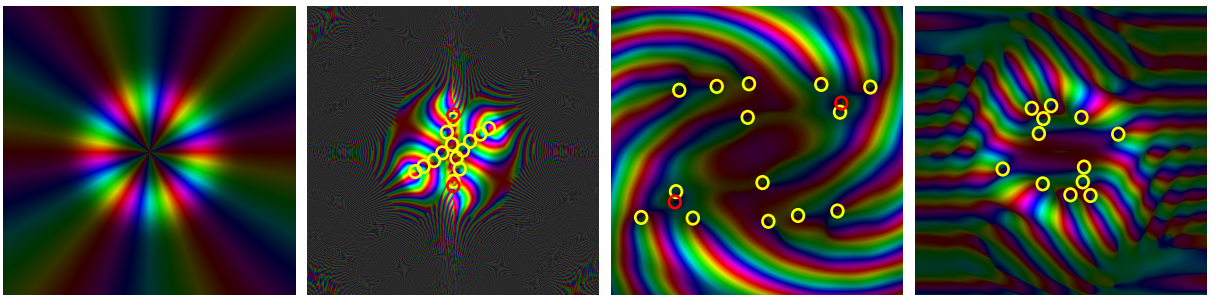


Figure 4.4: Phase profiles of LG_0^6 with highlighted singularities (positive - yellow, negative - red) in different stages of modulation. From left to right: untransformed input beam, LG_0^6 right after $\times 2$ -modulation with method B, then propagated over z_R , and lastly transformed by a lens.

are affected the most, since the magnitude of the coefficients for $p = 0$ and $p = 1$ is almost the same. Compared to the triangularly deformed method A, where the values jumped in multiples of 3, method B suffers from rectangular distortion and the coefficients spike in even indices l . Nonetheless, a similar problem is with the higher order modes $F_{\times 2}(LG_0^5), F_{\times 2}(LG_0^6), F_{\times 2}(LG_0^7)$, which do not have maximum in the targeted LG_0^{2l} , but the overlap is spread out between many different modes.

To summarise, OAM multiplication with method B is a slight improvement of the method A in terms of efficiency, yet it does not perform as intended. The modulated beams consist at most 30% out of the planned LG_0^{2l} modes and for the higher order modes it is significantly less. Table 4.3 tallying the coefficients demonstrates that a portion of the intensity is still unaccounted for. It is assumed to be in the coefficients with the higher l and p modes we did not compute. Contributions from the negative l modes are maximally 3% in total for the $F_{\times 2}(LG_0^1)$, while for the other modes they are around 1%. (The norm of the modulated beams is not precisely 1, because combining two halves together may cause a destructive interference in the vicinity of the vertical axis.)

$F_{\times 2}(\cdot)$	LG_0^0	LG_0^1	LG_0^2	LG_0^3	LG_0^4	LG_0^5	LG_0^6	LG_0^7
$\ \cdot\ ^2 =$	0.99	0.98	0.98	0.97	0.96	0.95	0.95	0.95
$\sum \alpha_{p,l} ^2 =$	0.92	0.90	0.91	0.90	0.90	0.88	0.84	0.79
$ \alpha_{0,2l} ^2 =$	0.34	0.33	0.31	0.24	0.15	0.07	0.03	0.02

Table 4.3: $\times 2$ -modulation with method B. The first row contains the square of the norm for the modulated beams $F_{\times 2}(LG_0^0), \dots, F_{\times 2}(LG_0^7)$. The sum of the coefficients from the plots in Fig.4.6 is given in the second row, while the last row shows only the targeted value $|\alpha_{0,2l}|^2$.

Dividing OAM by 2 with the beam splitter setup in Fig.1.10 seems to work the best of all the modulation methods. In Fig.B.3 the only defect of the $F_{/2}(LG_0^l)$ beams is the horizontal interference line, which vanishes with propagation. This is confirmed even by the Fourier decomposition in Fig.4.7, since the overlap of the modulated beams (after width-correcting lens with $f = 2.27 z_R$) with the $LG_0^{l/2}$ modes is around 80%. Only the size of the Gaussian beam could not be altered as much as the rest and thus part of the intensity is shared with the higher p coefficients.

Odd- l beams and their $/2$ -modulation are demonstrated in Fig.B.4. Method B has a beam splitter at its output and hence two separate beams are created, conversely to the near-perfect constructive interference in one output in the case of even l . To study the stability of these fractional OAM beams we let the $F_{/2}(LG_0^5)$ propagate in Fig.4.5. Each row of the zoomed out plots corresponds to one of the outputs, in which the lowermost left image in Fig.B.4 is propagated in the top row of Fig.4.5, and similarly the right output image in Fig.B.4 is evolved in the bottom row of Fig.4.5. The propagation distances are 1, 2, 4 multiples of Rayleigh range and infinity, respectively, going from left to right. At first glance it seems like the $/2$ -modulator divided LG_0^5 into $l = 3$ and $l = 2$, which propagate normally with only a little distortion. Nevertheless, the phase distribution is not completely uniform (some colors are missing). On top of that, the phase singularities seem to separate in the third inset below, which is evident even in the angular distribution illustrated in the last image.

It can be concluded that the $/2$ -modulation with method B is twice as efficient as method A and improves it in all regards, see Table 4.4. A square of the norm is comparable to the sum

of the Fourier coefficients for all the modulated beams except for the Gaussian. The problem with missing intensity of the $F_{/2}(LG_0^0)$, similar as in method A, can be resolved with additional computation of inner products with the higher- p modes. This time the contributions decrease faster, the value $|\alpha_{10,0}|^2$ is only 0.5 %.

Note that the norm in the first row of Table 4.4 is expectedly less than 1, since a small part of the intensity can be observed in the second output of the beam splitter (see Fig.1.11).

$F_{/2}(\cdot)$	LG_0^0	LG_0^2	LG_0^4	LG_0^6
$\ \cdot\ ^2 =$	0.88	0.94	0.94	0.87
$\sum \alpha_{p,l} ^2 =$	0.77	0.90	0.93	0.85
$ \alpha_{0,l/2} ^2 =$	0.56	0.78	0.87	0.81

Table 4.4: $/2$ -modulation with method B. The first row shows the norm for the modulated beams $F_{/2}(LG_0^0), \dots, F_{/2}(LG_0^6)$ with even l . The second row shows the sum of the coefficients from the plots in Fig.4.7, while the last row contains only the targeted value $|\alpha_{0,l/2}|^2$.

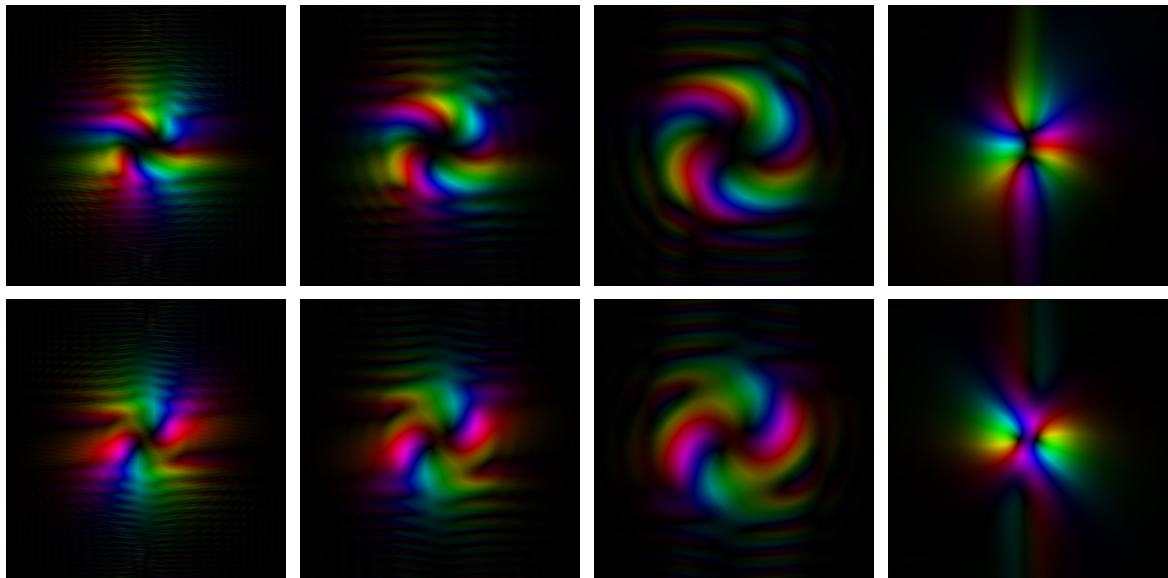


Figure 4.5: Propagation of both outputs from $/2$ -modulation of LG_0^5 . Each row corresponds to one of the two figures in Fig.B.4, but zoomed out to accommodate the whole beam. The distances are $z_R, 2z_R, 4z_R$ and infinity, respectively.

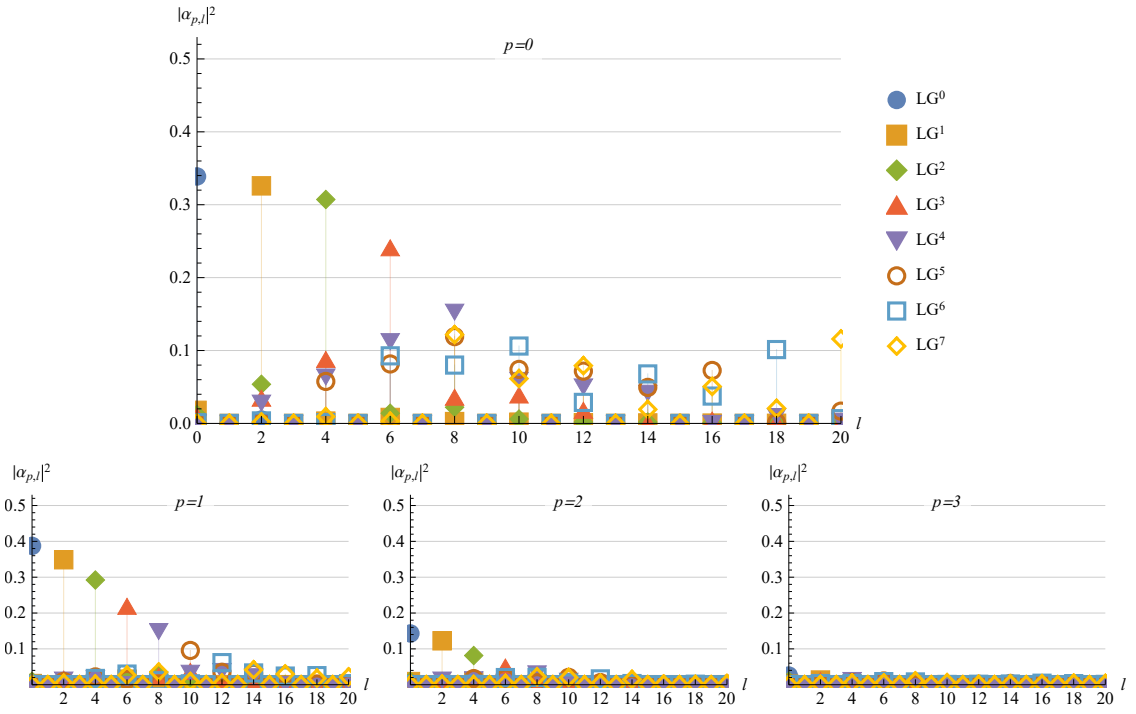


Figure 4.6: Method B: $F_{\times 2}(LG_0^l)$ beams after the width-correcting lens (i.e. the last column in Fig.B.3 and Fig.B.4) compared to standard LG_p^l modes.

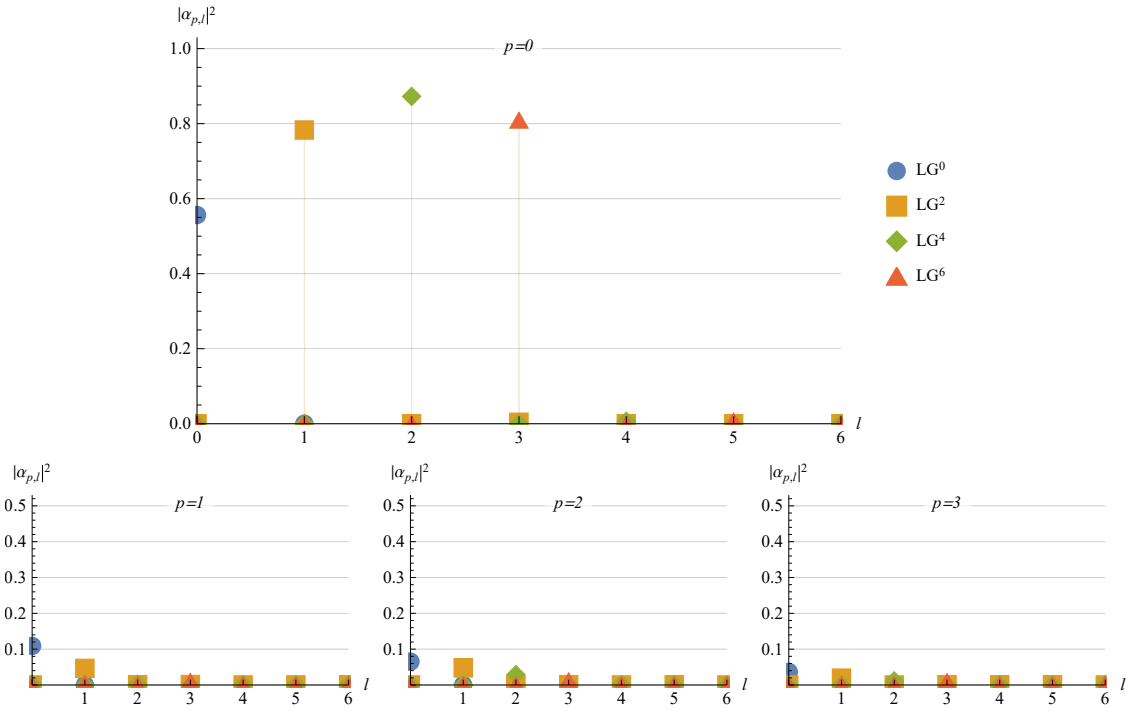


Figure 4.7: Method B: $F_{/2}(LG_0^l)$ beams after the width-correcting lens (i.e. the last column in Fig.B.3) compared to standard LG_p^l modes.

4.3 $\pm\delta$ holograms

The other key arithmetic operation with OAM is addition/subtraction of a constant. According to Section 1.4 we have multiple choices of optical elements for such operation, but since the previous methods utilize solely computer generated holograms, we will ignore the binary gratings and study just the $\pm\delta$ -filter implemented by spatial phase modulation.

With the notation defined in Section 2.4 the effect of the hologram can be expressed as

$$F_\delta(LG_p^l) = LG_p^l e^{i\delta\varphi}. \quad (4.2)$$

Similarly to the previous sections, the efficiency of this operation is calculated with decomposition of the transformed beam into the basis of LG modes according to (4.1). As before, we will investigate the 3 qubit modes LG_0^0, \dots, LG_0^7 only. Although the operation produces the correct phase distribution, the radial distance is retained from the input beam. The incorrect width of the beams causes LG modes with higher p to emerge in the decomposition, yet all of them with the appropriate azimuthal index $l + \delta$. In other words, the overlap of the $F_\delta(LG_0^l)$ with beams $LG_p^{\tilde{l}}$ will be 0 for all \tilde{l} other than $\tilde{l} = l + \delta$.

The results of our numerical computations of the inner products between $F_\delta(LG_0^l)$ and $LG_0^{l+\delta}$ for $l \in \{0, \dots, 7\}$ and $\delta \in \{-4, \dots, 4\}$ are shown in Fig.4.8. The added/subtracted value δ is not directly provided in the figure, but is implied by the horizontal axis. Since our quantum optical gates utilize only positive azimuthal indices, the inner products for every input beam LG_0^l are computed only if $l + \delta \geq 0$. Even though the filter F_0 does not modulate the beam in any way and hence gives 100% overlap with LG_0^{l+0} , we still included it in our illustration to bridge between the data with positive and negative δ . For the same reason of easier orientation, all markers for a specific input beam are connected with a polyline.

As was discussed above, the larger the difference in azimuthal indices of the input and output beams, the more apparent the changes in beams diameter become. Therefore as the magnitude of δ increases, the efficiency of the hologram decreases, as seen in Fig.4.8. The most affected is the LG_0^0 mode, since the overlap is calculated right after the $\pm\delta$ -modulator and the beam is still shaped as a Gaussian. Conversely, the widest LG_0^7 the filter performs noticeably better, even the transformation $F_{-4}(LG_0^7)$ has around 50% of intensity in the expected mode LG_0^3 .

It turns out the inner products can be straightforwardly calculated even analytically. First, we introduce the symbol $\eta_l(\delta)$, which represents the efficiency of the F_δ hologram with a given input LG_0^l as a function of the added/subtracted constant δ . (Notice that $\eta_l(\delta) = |\alpha_{0,l+\delta}|^2$ in Fig.4.8.) Second, we prepare

$$\begin{aligned} \langle F_\delta(LG_0^l) | &= \sqrt{\frac{2}{\pi l!}} (\sqrt{2}r)^l e^{-r^2} e^{-il\varphi} e^{-i\delta\varphi} \\ |LG_0^{l+\delta}\rangle &= \sqrt{\frac{2}{\pi(l+\delta)!}} (\sqrt{2}r)^{l+\delta} e^{-r^2} e^{i(l+\delta)\varphi}, \end{aligned} \quad (4.3)$$

where $l \geq 0$, $l + \delta \geq 0$ and we took $w_0 = 1$ for simplicity (the choice of w_0 does not affect the result). Finally, everything can be put together and the efficiency $\eta_l(\delta)$ expressed as

$$\begin{aligned}
\eta(\delta) &= \left| \langle LG_0^l e^{i\delta\varphi} | LG_0^{l+\delta} \rangle \right|^2 \\
&= \left(\frac{2^{l+\frac{\delta}{2}+1}}{\pi\sqrt{l!}\sqrt{(l+\delta)!}} \int_0^\infty \int_0^{2\pi} r^{2l+\delta} e^{-2r^2} e^{i0\varphi} r \, dr \, d\varphi \right)^2 \\
&= \frac{2^{2l+\delta+4}}{l!(l+\delta)!} \left(\int_0^\infty r^{2l+\delta+1} e^{-2r^2} \, dr \right)^2 \\
&= \frac{2^{2l+\delta+4}}{l!(l+\delta)!} \left(\frac{1}{2^{l+\frac{\delta}{2}+2}} \int_0^\infty t^{l+\frac{\delta}{2}} e^{-t} \, dt \right)^2 \\
&= \frac{\Gamma(l+\frac{\delta}{2}+1)^2}{l!(l+\delta)!}.
\end{aligned} \tag{4.4}$$

One could check that the final result gives indeed the same values as plotted in Fig.4.8.

In those cases in which each $\pm\delta$ -filter transforms one specific LG mode, the efficiency can be greatly improved by adjusting the size of the output beam with a telescopic lens setup. The characteristic diameter of the beam is proportional to the factor $\sqrt{2p+|l|+1}$ [39], and thus the telescope needs to magnify by a factor of

$$\frac{f_o}{f_i} = \frac{\sqrt{|l+\delta|+1}}{\sqrt{|l|+1}}, \tag{4.5}$$

where f_0 and f_i are the focal lengths of the object and image lens, respectively. Nonetheless, such correction will never be 100% effective because the particular functional dependence of amplitude on the radial coordinate also changes depending on l and common lenses cannot rectify that.

To better illustrate the idea, an example is in order. Take our design of C_1NOT_3 gate implemented with parity sorters and 3 OAM qubits only. (Were there more than 3 qubits, each arm of the 3 stage parity sorter would contain a superposition of several modes and the proposed upgrade would not perform as intended.) The gate, symbolically given by (3.19), contains two F_{+4} and two F_{-4} filters each transforming only one LG component each, i.e. $F_{+4}(LG_0^1)$, $F_{-4}(LG_0^5)$, $F_{+4}(LG_0^3)$ and $F_{-4}(LG_0^7)$. Table 4.5 provides numerical values of the Fourier coefficients for the plain application of the filters in the first row compared to the width adjusted beams (with the corresponding lenses for each transformation) in the second row. Evidently, including a few lenses in our optical C_1NOT_3 gate design can boost the efficiency to at least 85%.

	$F_{+4}(LG_0^1)$	$F_{-4}(LG_0^5)$	$F_{+4}(LG_0^3)$	$F_{-4}(LG_0^7)$
$ \alpha_{0,l+\delta} ^2 =$	0.3	0.3	0.48	0.48
width-adjusted $ \alpha_{0,l+\delta} ^2 =$	0.85	0.85	0.94	0.94

Table 4.5: Efficiency of the C_1NOT_3 gate implemented with parity sorters on 3 qubits. First row shows the magnitude of the Fourier coefficients $|\alpha_{0,l+\delta}|^2$ calculated right after the filter $F_{\pm 4}$ for the intended input beams. On the contrary, the second row illustrates an improved design by including width-correcting set of lenses after the filters in each arm.

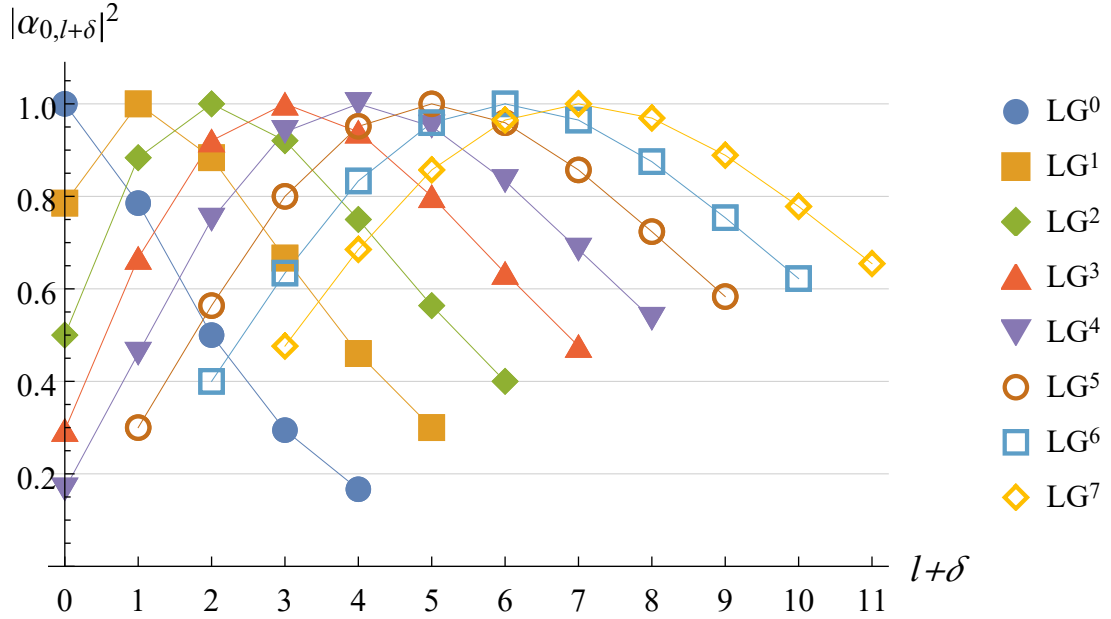


Figure 4.8: Calculated efficiency of the OAM addition/subtraction filters F_δ given by (4.2) for input beams LG_0^0, \dots, LG_0^7 . The inner products are computed between $LG_0^l e^{i\delta\varphi}$ and $LG_0^{l+\delta}$ for $\delta \in \{-4, \dots, 4\}$ if $l + \delta \geq 0$.

4.4 Efficiency of optical quantum gates

Based on the data from the previous sections we can now determine how lossy the individual quantum gates from Chapter 3 are. First, the bitwise operations like shifters and swaps are examined. Second, we study the efficiency of the single qubit gates with respect to the position of the affected qubit, and in the end details for implementing the *CNOT* gate with parity sorters are provided.

An immediate observation concerning all gates can be made right at the beginning. Efficiency of consequent operations is calculated as a product of the individual efficiencies. On the other hand, there are many occasions in which elements are located in parallel optical channels. If that is the case, we approximate the lower boundary of the throughput of the whole set of parallel operations with the efficiency of the worst performing one.

The design of our right shifter is illustrated in Fig.2.1. The device starts with a parity sorter PS_π , which comprises two beam splitters and a beam rotator. All these basic elements are theoretically perfect, but a practical efficiency of the whole parity sorter is estimated to be 83% including reflection losses on the beam splitters and Dove prisms (acting as rotators) [23]. From now on we assume that all parity sorters will have this throughput regardless of the orientation and the angle of rotation.

A consequent element in the right shift operation is the F_{-1} filter. Its efficiency can be seen in Fig.4.8 for different inputs and we will take the lowest value, that is 0.79. Finally, there are two $/2$ -modulators in parallel which can be implemented with either method A or B. From the results in Sections 4.1 and 4.2 it is clear that the method B performs better despite the more complex design. Therefore the efficiency of the OAM division is 56% as seen in Table 4.4.

In total, the throughput of a single right shifter is approximately $0.83 \times 0.79 \times 0.56 = 0.37$.

Shifting qubits to the right is usually accompanied by the inverse operation, the left shift, designed in Fig.2.2. It consists of one inverted parity sorter with efficiency of 83 %, one F_{+1} filter with the lowest efficiency 0.79, and two OAM doubling modulators. Although the calculated efficiency of the $\times 2$ -modulation with method B (seen in Table 4.3) is overall abysmal, it can be improved by limiting our experiment to 3 qubits and complying to the rule that every left shift needs to be preceded by a right shift. Accordingly, the only inputs of the $\times 2$ -modulator are the modes LG_0^0, \dots, LG_0^3 and the lowest efficiency for them is 24 %.

Overall, the right shifter with limited input to modes with $l \in \{0, \dots, 3\}$ has a throughput $0.24 \times 0.79 \times 0.83 = 0.16$ and performs more than two times worse as its inversion. Hence the shifters should be avoided and used only if no other alternative exists.

The swap operation is useful for repositioning certain qubits in the OAM bit string. It can be implemented either with a series of right and left shifters or with parity sorters. Following our own advice we focus only on the second method.

Typically it is laborious to design a swap S_{mn} for general positions m and n of the bits. (Note that $S_{mn} = S_{nm}$.) Nevertheless we developed universal formulae for the number of optical elements from which we can derive an approximate efficiency of the swap dependant on m and n . Let us start with the Mach-Zehnder interferometers. The larger of the two indices in S_{mn} indicates how many stages of the OAM sorters are needed to reach that position. More precisely, the total number of MZI is equal to

$$2 \times \left(2^{\max\{m,n\}} - 1 \right), \quad (4.6)$$

where the whole expression is multiplied by 2 because there are the forward and the inverse sorters. However, most of the MZI are in parallel channels and only $2 \times \max\{m,n\}$ of them are in series. The total contribution to the losses of S_{mn} operation caused by interferometers is thus $0.83^{2 \times \max\{m,n\}}$.

Several OAM addition/subtraction filters are situated between the parity sorters. Even though all of $F_{\pm\delta}$ holograms are in parallel, their total number given by

$$2^{\max\{m,n\}-1} \quad (4.7)$$

may still be useful for the overview like Table 2.1. More important is the difference in OAM the $F_{\pm\delta}$ filters provide. By generalization of a few simple cases of S_{mn} we derived the expression

$$|\delta| = \sum_{k=1}^{|m-n|} 2^{\max\{m,n\}-1-k}. \quad (4.8)$$

The actual efficiency of $F_{\pm\delta}$ for the given δ was computed in (4.4) for general input LG_0^l , however, we are only interested in the lower boundary of the efficiency. The worst case scenario for $\eta_l(\delta)$ is calculated with the input LG_0^1 , because the most lossy LG_0^0 mode (equivalent to a bit string of only zeros) is never transformed in a swap. Therefore, with $l = 1$ in $\eta_l(\delta)$ we get

$$\eta_1(\delta) = \frac{\Gamma\left(\frac{\delta}{2} + 2\right)^2}{(\delta + 1)!}, \quad (4.9)$$

in which one can substitute (4.8).

The list of optical elements in the swap operation is completed by stating that there are no $\times 2$ -, $/2$ -modulators, and one needs to prepare $2^{\max\{m,n\}}$ independent optical channels.

Putting everything together the final efficiency of a general swap S_{mn} can be approximated by

$$0.83^{2 \times \max\{m,n\}} \times \eta_1 \left(\sum_{k=1}^{|m-n|} 2^{\max\{m,n\}-1-k} \right). \quad (4.10)$$

The quantum operations can be examined in a similar fashion. Single qubit gates are made of two parity sorters and some additional elements in between. The most lossy one (out of our designs for $X, Y, Z, H, S, T, R_x, R_y, R_z$) is probably the Hadamard gate given by Fig.3.5 and we will consider its efficiency as a representative for all the others. It comprises two $F_{\pm 1}$ filters in series and a beam splitter. The beam splitter is expected to behave the same as the ones in the parity sorter and therefore the total throughput of the Hadamard gate is approximately $0.83 \times 0.79 \times 0.83 \times 0.79 \times 0.83 = 0.36$.

The previous paragraph was concerned with single qubit gates affecting the most easily accessible qubit. To reach other positions we have an option to either shift the qubits several times, or to perform a swap.

Say the targeted qubit is in n th position from the right. Then the first method requires to shift $(n-1)$ times to the right, apply the single qubit gate, and left shift $(n-1)$ times back. (We note that each right shift creates two outputs and thus the quantum gate needs to be implemented 2^{n-1} times in parallel channels.) In total, the efficiency of performing a single qubit operation on n th position with the help of shifters is $0.24^{n-1} \times 0.36 \times 0.16^{n-1}$, where we assumed the worst case scenario with the Hadamard gate.

In contrast, the second option suggests to first swap the qubits with S_{1n} , then execute the quantum operation and finally swap back again with $S_{n1}(=S_{1n})$. The combined throughput of these steps is computed by squaring the value in expression (4.10) and multiplying it by the efficiency of the given quantum gate. Whether the swap method is superior over the shifting one depends on the position n and how well the filters $F_{\pm \delta}$ in S_{1n} perform.

Lastly we study the efficiency of the *CNOT* operation. Although Section 3.3 presented many possible designs, the only *CNOT* gate not utilizing shift operations is the one with parity sorters. (One could argue that for example the C_1NOT_3 with S_{23} given by (3.17) could use only swaps with parity sorters and no shifters. However, then it would be simpler to directly execute the C_1NOT_3 with only one parity sorter according to (3.19) and not bother with the swaps at all.)

Following the same structure as with the swap operations, it is possible to calculate the precise amount of optical elements for a general C_mNOT_n gate with the control qubit in m th position and the target in n th position. The number of Mach-Zehnder interferometers depends on the maximum of the numbers m and n but can be lowered based on the position of the target. The full expression given by

$$\begin{cases} 2 \times (2^{\max\{m,n\}} - 1), & \text{for } m > n, \\ 2 \times (2^{\max\{m,n\}} - 1) - \sum_{k=1}^{n-m} 2^{n-k}, & \text{for } m < n \end{cases} \quad (4.11)$$

was deduced from the simplest cases of all possible C_mNOT_n gates on 4 qubits. Despite the convenient reduction in the amount of MZI, the total efficiency of the parity sorters is still $0.83^{2 \times \max\{m,n\}}$, since all the savings happen on parallel channels.

The number of required $F_{\pm \delta}$ filters for C_mNOT_n is the same as for the swap operation, that is

$$2^{\max\{m,n\}-1}. \quad (4.12)$$

On the other hand, the value δ itself can be calculated from the position of the target qubit with the expression

$$|\delta| = 2^{n-1}, \quad (4.13)$$

from which we can approximate its throughput with the formula (4.9).

The list of necessary equipment is finished with the fact that there are no $\times 2$ -, $/2$ -modulators and, additionally, the operation will span over $n_{\text{MZI}}/2 + 1$ optical channels, where n_{MZI} is the amount of Mach-Zehnder interferometers taken from (4.11).

Given the above, the estimated lower boundary for the efficiency of the $C_m NOT_n$ gate can be computed with

$$0.83^{2 \times \max\{m,n\}} \times \eta_1(2^{n-1}). \quad (4.14)$$

Neither the swap S_{nm} nor the $C_m NOT_n$ operations seem very practical in terms of throughput for large indices n and m . Nonetheless, assuming the experiment is performed with limited and controlled amount of LG modes, one could improve the inefficient holograms with large δ by including width adjusting lenses as was suggested at the end of the previous section.

Conclusion

The goal of this thesis was to introduce optical logic operations on paraxial beams carrying an orbital angular momentum. The main contributions are the $\times 2$ - and $/2$ -modulators capable of doubling and halving OAM. We present two possibilities for their implementation: method A is a straightforward coordinate transformation, shown in Fig.1.7, with a downside of reduced throughput due to the phase-amplitude modulators. On the contrary, method B improves on the inefficiency at the cost of more a complicated setup illustrated in Fig.1.10.

The performance of both operations is studied in Chapter 4 with numerical simulations on the first few LG modes. While the $/2$ -modulator behaves as intended and transforms around 80 % of the incoming intensity into the correct $LG_0^{l/2}$ mode (with method B), the $\times 2$ -modulator introduces unexpected distortions and its efficiency, in the best case scenario (with method B), reaches barely 30 %. The triangular deformation of the output is especially evident on the higher l modes in method A, see Fig.B.1 and Fig.B.2. We attribute the misshaped outputs to the $\tilde{\Phi}_{(\times 2)}$ hologram illustrated in Fig.A.2a), which indicates a $\frac{2}{3}\pi$ rotational symmetry. Similarly, method B is adapted from method A and suffers from analogous deformation, this time rectangular (as seen in Fig.B.3 and Fig.B.4).

Moreover, the applicability of the $\times 2$ - and $/2$ -modulators is also limited by the width of the transformed beams. Since the transverse dimensions of LG modes are proportional to the factor $\sqrt{|l|+1}$ (for $p=0$), the aperture size and resolution of our light modulators pose obvious restrictions on the number of viable input modes.

As can be seen, the suggested methods for doubling and halving OAM are not very efficient. Nevertheless, they are the key components in the proposed classical logic operations, namely the shifters, acting on strings of bits encoded in OAM (by expressing the azimuthal index l in base 2). We put forward designs for the right and left shift illustrated in Fig.2.1 and Fig.2.2, respectively, as well as detailed description of what happens to the last extracted/injected bit.

The next studied classical operation is the swap of two arbitrary bits, with an example shown in Fig.2.4. The main components are the parity sorters capable of sending a beam in one of the two optical output channels depending on the parity of their OAM, and the $F_{\pm\delta}$ filters adding/subtracting a constant δ to the OAM. Despite not utilizing the inefficient $\times 2$ - and $/2$ -modulators, the throughput of the swap estimated in (4.10) is still very low if the targeted bits are far in the string or are far apart from each other.

Thanks to the linearity of all the components, our concepts work on superpositions of beams with different OAM and thus can be used for manipulating quantum information. The orthonormal LG modes with the binary representation of the integer $l \in \{0, \dots, 2^n - 1\}$ form a natural basis for n qubits, which are transformed with linear optical quantum gates. We created designs for the Pauli rotations in Fig.3.2, for the most common operations X, Y, Z, H, S, T in Fig.3.3, Fig.3.4, Fig.3.5, and for a general $CNOT$ gate (examples in Fig.3.6 and Fig.3.7), covering a

well-known universal set. Theoretical efficiencies of the gates are presented in Chapter 4, along with a complete list of required elements to construct the *CNOT* on arbitrary control and target qubits.

Although the quantum operations theoretically manipulate OAM, they do not affect it directly. Instead the presented gates first transform the information from the OAM qubits into position qubits on 2^n optical paths, then perform the operation, and finally convert the result back into OAM. Unless the numerous parity sorters (consisting of Mach-Zehnder interferometer and a beam rotator) become commercially available as integrated optical devices without the need for alignment, it would be easier to directly work with the position qubits the whole time and transform between the degrees of freedom only at the beginning and at the end of the quantum protocol.

A subsequent work could improve on our $\times 2$ modulators and attempt to eliminate the triangular deformation, probably by revamping the phase functions or by utilizing unconventional elements like astigmatic lenses. It would also be interesting to recreate the suggested designs in an actual physical experiment and compare the results to our numerical simulations.

However, we see the most promising development in the application of OAM as multidimensional state spaces. There are already many research groups investigating optical qudits and pursuing generalized quantum gates [23, 27, 28, 38], but to our knowledge none took the direction explored here.

Appendix

A. Materials and Methods

The modelled phase profiles, like in Fig.1.8, Fig.B.1 and others, were created in Wolfram Mathematica version 12.1. Each plot is a discretization of a scalar field distribution in a plane perpendicular to the direction of propagation. The data about the beam is stored in a 501×501 grid of complex numbers and every operation we would want to perform on the beam is adapted for this matrix. The colour of every point is determined by the argument of the complex value the optical field has in those coordinates, while the brightness is directly proportional to its magnitude.

The input is always a LG mode calculated from the equation (1.6) at $z = 0$ with the waist parameter w_0 set to 1/10 of the grid dimension (i.e. 50 pixels). In our model, the waist represents the basic unit of measurement. Defining $w_0 = 1$, the plot range is then spanned from $-5w_0$ to $+5w_0$ in both directions and divided into segments $dx = 0.02w_0$. The size was chosen for the beam to fit inside the sampled area and to leave room around for evolution, see the first image in Fig.A.1 illustrating LG_0^2 . However, in few cases with beams of higher order which widen too rapidly, a plot of size $(-10, 10) \times (-10, 10)$ was needed to accommodate the whole beam.

Modulators are implemented as matrices with $\Phi(0,0)$ aligned in the centre of the matrix. Hence, sending a beam through a modulator is equivalent to multiplying the data grid by the modulator matrix element-wise. The phase function $\tilde{\Phi}_{(\times 2)}$ given by (1.10) is illustrated in the first image of Fig.A.2, the inset b) shows the phase correcting function $\Psi_{(\times 2)}$ given by (1.11).

Our OAM transformation setup is assembled from two modulators (the second only corrects the phase) and a lens, see Fig.1.7 and Fig.1.10. Since the first modulator is positioned in the first focal plane and its intended output is displayed in the second focal plane, the lens essentially performs a Fourier transformation [40, p. 106]. Discrete Fourier transformation is easily implemented as a matrix multiplication by a Fourier matrix, where rows and columns of 2-dimensional data are transformed independently. The physical parameters k and f , which appear in the modulator function, were fixed as $k/f = 8w_0^{-2}$, which can be written as $f = 0.25 z_R$.

Free space propagation in the near field is governed by the Fresnel diffraction integral [22]. The formula can be viewed as a convolution

$$U_2(x, y, z) = \frac{ke^{ikz}}{2\pi iz} \left(U_1(x, y, 0) * \exp \left[\frac{ik}{2z}(x^2 + y^2) \right] \right) \quad (\text{A.1})$$

and Mathematica already has an implementation of discrete convolution. We usually evaluate the Fresnel integral at multiples of Rayleigh range and since $z_R = 1/2kw_0^2$, the wave number cancels out (apart from the global phase factor e^{ikz}) and the only parameter left is the waist w_0 .

Moreover, propagating a beam introduces a wavefront curvature in the form

$$\exp \left[\frac{ik}{2R(z)}(x^2 + y^2) \right], \quad (\text{A.2})$$

where the radius is defined by equation (1.8). To correct this unwanted deformation we display our propagated beams with extra phase factor negating the curvature and making our plots uniform. One can, for instance, use a lens with focal length $f = R(z)$, because passing a beam through a lens adds exactly $\exp \left[-\frac{ik}{2f}(x^2 + y^2) \right]$ [22]. We also ignore the global phase e^{ikz} responsible only for rotation of the whole beam in our plots, see Fig.A.1.

Sections 4.1 and 4.2 require a computation of inner product $\langle p, l | \psi \rangle$. In our matrix representation of the functions we use the Frobenius inner product for matrices

$$\langle A | B \rangle = \text{Tr}(A^\dagger \cdot B). \quad (\text{A.3})$$

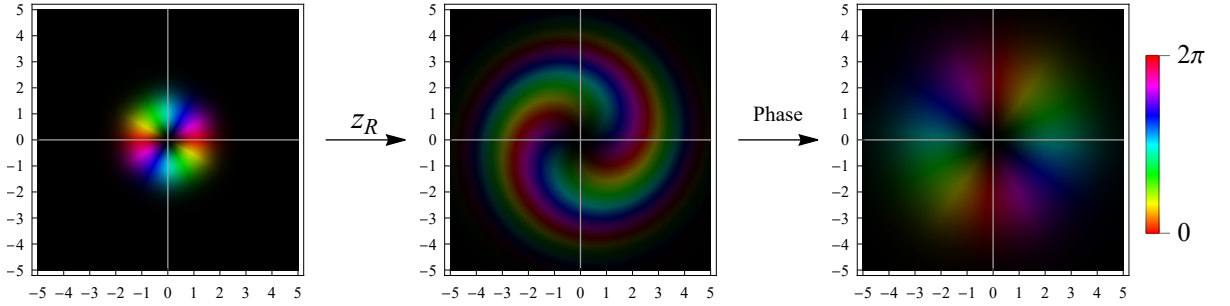


Figure A.1: LG_0^2 beam propagated over distance z_R with the full Fresnel integral (A.1) and after phase correction.

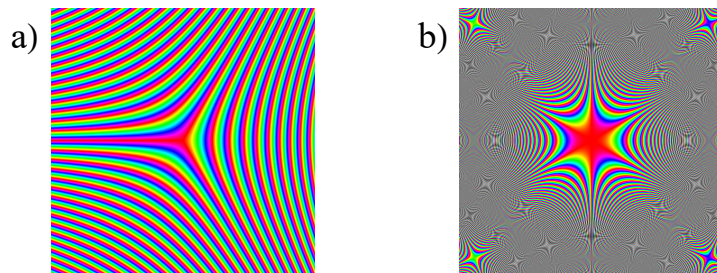


Figure A.2: a) The phase functions $\tilde{\Phi}_{(\times 2)}$ given by (1.10). b) The phase function $\Psi_{(\times 2)}$ given by (1.11).

B. Plots of numerical simulations

Sections 1.4, 4.1 and 4.2 are concerned with $\times 2$ - and $/2$ -modulators. The next four pages contain plots of LG modes for 3 qubits (LG_0^1, \dots, LG_0^6) transformed by the modulators with methods A and B, and how they propagate. Mode LG_0^0 is left out because it is not very interesting, and similarly transformations of LG_0^7 would reveal nothing new that the LG_0^5 would not show already. We took the standpoint that for illustration purposes it is better to present fewer but larger plots than scale down the figures to display as many of them on one page as possible. In addition, brightness is adjusted as well, since some of the plots would otherwise be too dark. Figures marked with “+” have the intensity increased more than the rest to show anything at all.

Figure B.1 and B.3: Transformations of the even- l valued beams LG_0^2, LG_0^4, LG_0^6 with method A and B, respectively. The first column plots the original beam right before the modulator. The second column is the output of each beam after the $\times 2$ -modulator in the top row, and after $/2$ -modulators in the bottom row (only the beam splitter output with constructive interference is shown). Subsequent plots contain the outputs from the second column propagated over distance z_R . Last column displays the Fourier image of the second column, which is equivalent to letting the beam propagate to infinity and plotting the angular distribution. We used a focal length of $f = 0.5 z_R$ for the $\times 2$ -modulated beams and $f = 2.27 z_R$ for the $/2$ -modulated beams in order to match the width of the beams to the targeted LG_0^{2l} and $LG_0^{l/2}$, respectively.

Figure B.2 and B.4: Transformations of the odd- l valued beams LG_0^1, LG_0^3, LG_0^5 with method A and B, respectively. The $\times 2$ -modulated beams in the first rows follow the same logic as the even- l beams in even cases. The bottom row of each beam plots what would happen if we tried to divide odd- l beams by 2. Method A with a single output from the modulator illustrates beams without any clear phase gradient. As they propagate, their intensity is rapidly lost and therefore we had to boost the brightness of the figures to even see the result (“+” symbolizes we multiplied the data by 4 prior to plotting). On the other hand in case of method B, the two figures show both outputs of the beam splitter present in the modulator in Fig.1.10, in which no destructive interference occurs, conversely to the even- l beams.

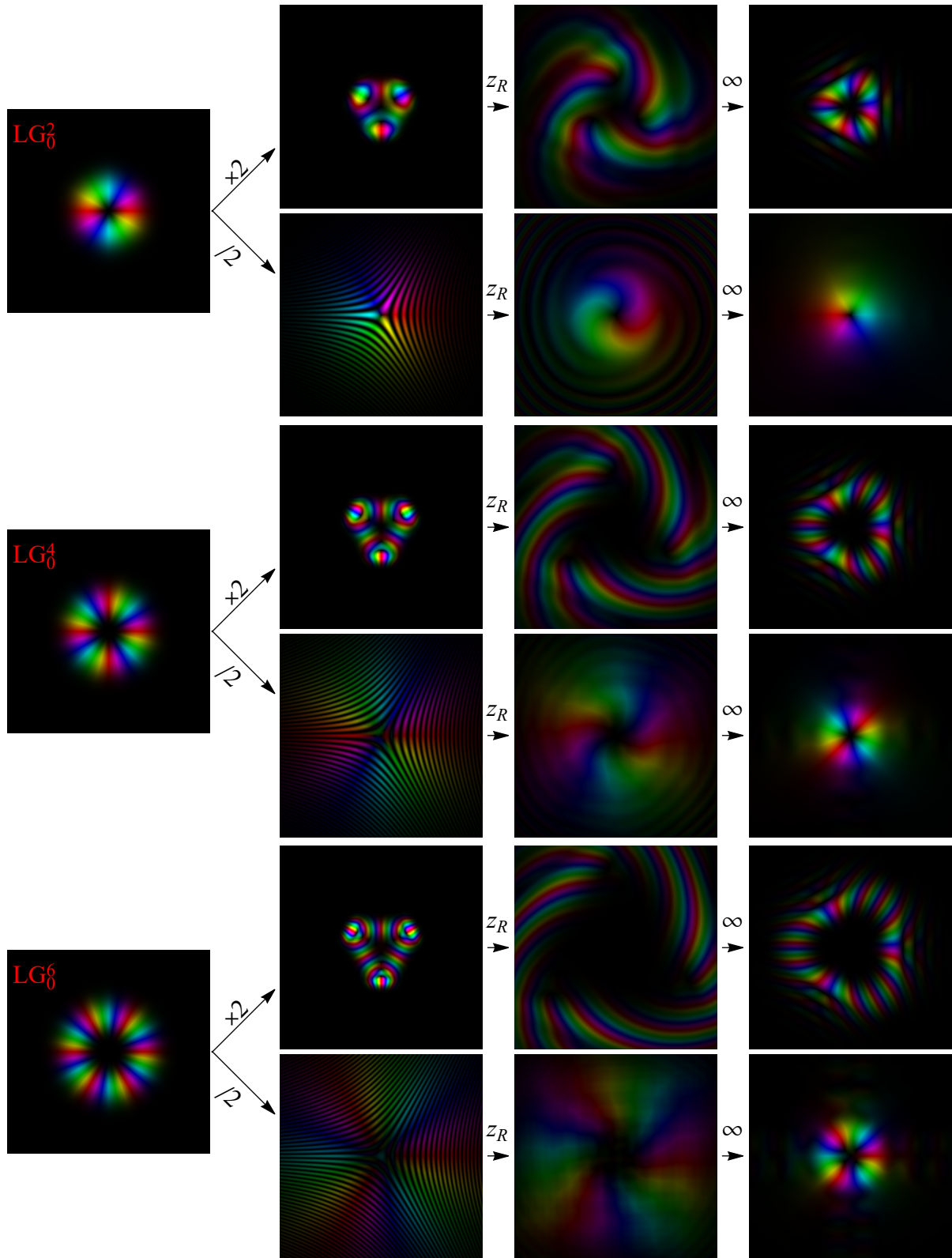


Figure B.1: Method A: transformations of LG_0^2 , LG_0^4 , LG_0^6 . Detailed description is given at the beginning of Appendix B.

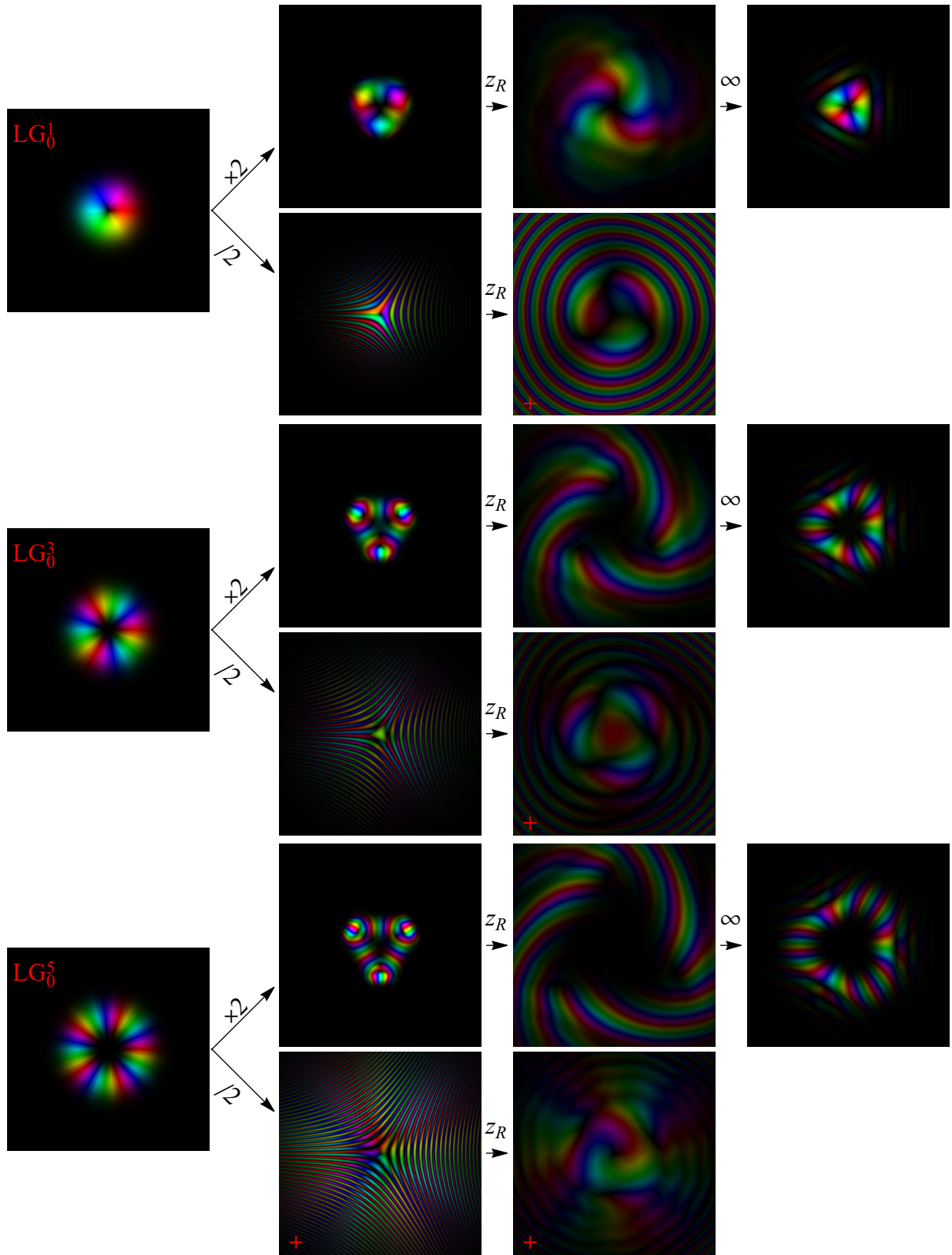


Figure B.2: Method A: transformations of LG_0^1 , LG_0^3 , LG_0^5 . Detailed description is given at the beginning of Appendix B.

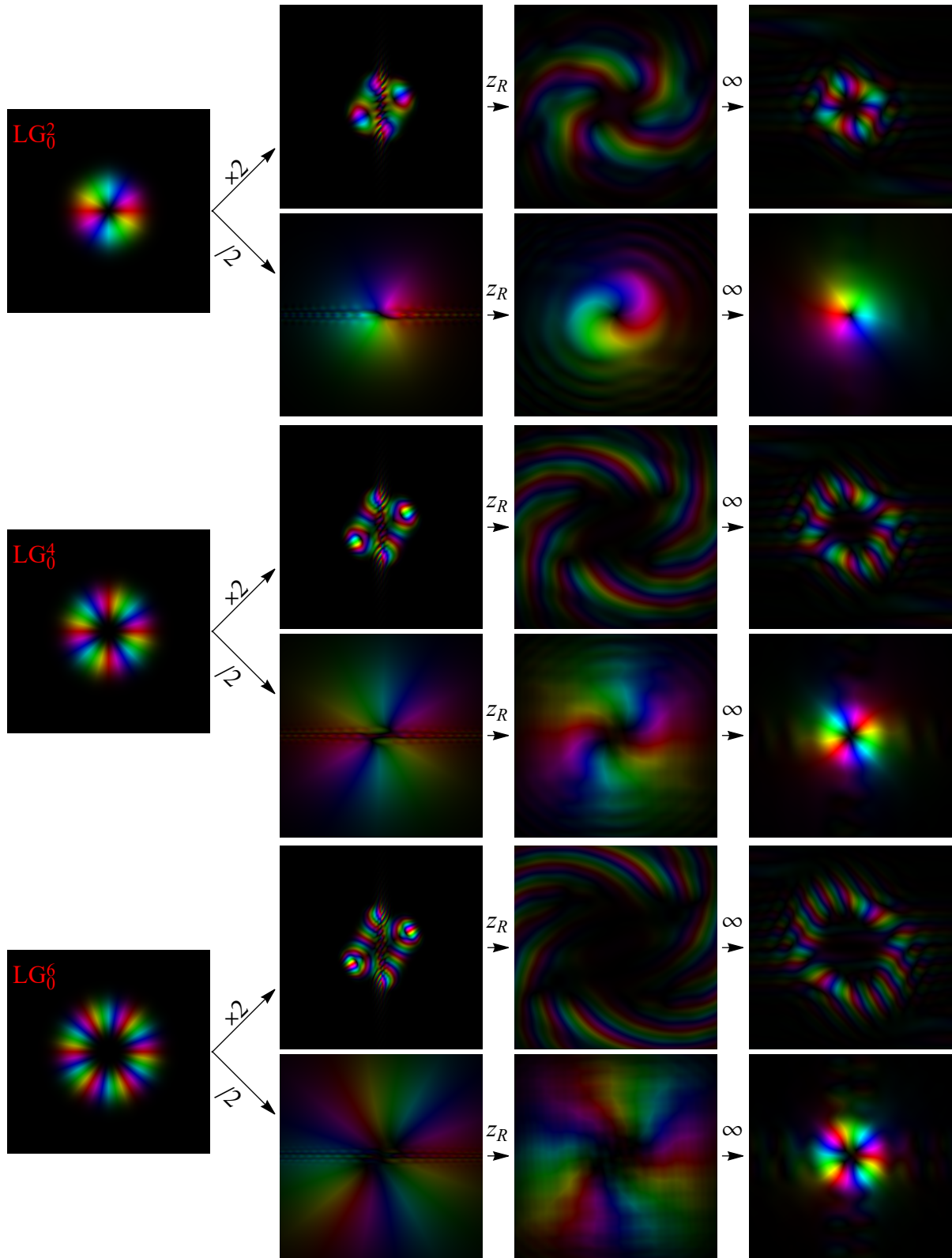


Figure B.3: Method B: transformations of LG_0^2 , LG_0^4 , LG_0^6 . Detailed description is given at the beginning of Appendix B.

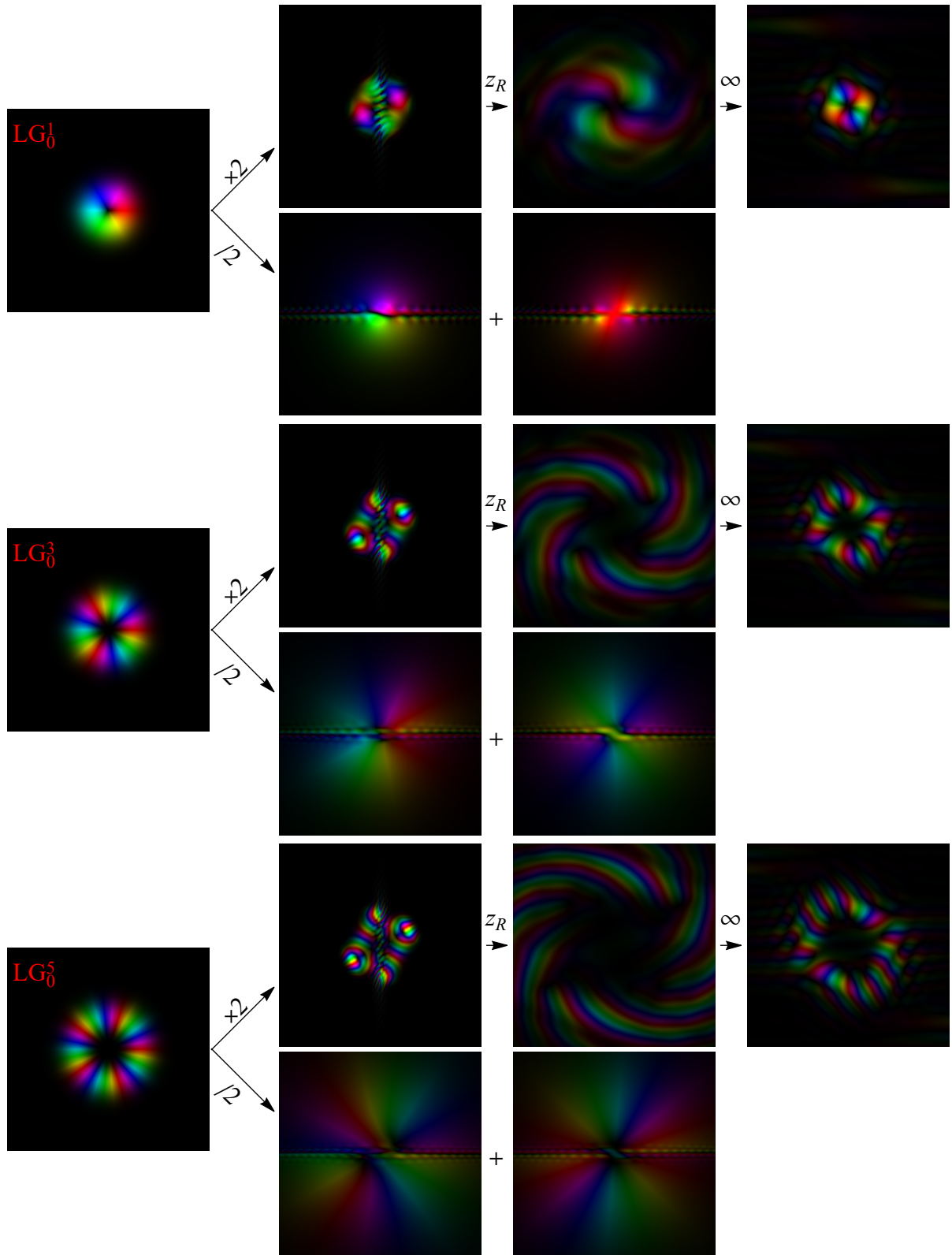


Figure B.4: Method B: transformations of LG_0^1 , LG_0^3 , LG_0^5 . Detailed description is given at the beginning of Appendix B.

Bibliography

- [1] Allen, L., Beijersbergen, M. W., Spreeuw, R. J. C., & Woerdman, J. P. (1992). Orbital angular momentum of light and the transformation of Laguerre-Gaussian laser modes. *Physical Review A*, *45*(11), 8185–8189. <https://doi.org/10.1103/physreva.45.8185>
- [2] Allen, L., Padgett, M. J., & Babiker, M. (1999). The Orbital Angular Momentum of Light. *Progress in Optics*, *39*, 291–372. [https://doi.org/10.1016/s0079-6638\(08\)70391-3](https://doi.org/10.1016/s0079-6638(08)70391-3)
- [3] Molina-Terriza, G., Torres, J. P., & Torner, L. (2001). Management of the Angular Momentum of Light: Preparation of Photons in Multidimensional Vector States of Angular Momentum. *Physical Review Letters*, *88*(1). <https://doi.org/10.1103/physrevlett.88.013601>
- [4] Padgett, M., & Bowman, R. (2011). Tweezers with a twist. *Nature Photonics*, *5*(6), 343–348. <https://doi.org/10.1038/nphoton.2011.81>
- [5] Wang, J., Yang, J.-Y., Fazal, I. M., Ahmed, N., Yan, Y., Huang, H., Ren, Y., Yue, Y., Dolinar, S., Tur, M., & Willner, A. E. (2012). Terabit free-space data transmission employing orbital angular momentum multiplexing. *Nature Photonics*, *6*(7), 488–496. <https://doi.org/10.1038/nphoton.2012.138>
- [6] Yao, A. M., & Padgett, M. J. (2011). Orbital angular momentum: origins, behavior and applications. *Advances in Optics and Photonics*, *3*(2), 161. <https://doi.org/10.1364/aop.3.000161>
- [7] Mair, A., Vaziri, A., Weihs, G., & Zeilinger, A. (2001). Entanglement of the orbital angular momentum states of photons. *Nature*, *412*(6844), 313–316. <https://doi.org/10.1038/35085529>
- [8] Deng, L.-P., Wang, H., & Wang, K. (2007). Quantum CNOT gates with orbital angular momentum and polarization of single-photon quantum logic. *Journal of the Optical Society of America B*, *24*(9), 2517. <https://doi.org/10.1364/josab.24.002517>
- [9] Nagali, E., Sciarrino, F., De Martini, F., Marrucci, L., Piccirillo, B., Karimi, E., & Santamato, E. (2009). Quantum Information Transfer from Spin to Orbital Angular Momentum of Photons. *Physical Review Letters*, *103*(1). <https://doi.org/10.1103/physrevlett.103.013601>
- [10] Erhard, M., Fickler, R., Krenn, M., & Zeilinger, A. (2017). Twisted photons: new quantum perspectives in high dimensions. *Light: Science & Applications*, *7*(3), 17146–17146. <https://doi.org/10.1038/lsa.2017.146>
- [11] Siegman, A. E. (1986). *Lasers*. University Of Science Books.

- [12] Staněk, M. (2019). *Orbitální moment hybnosti světla/Orbital Angular Momentum of Light* [Unpublished bachelor's thesis, in Czech]. ČVUT FJFI. Available from <http://physics.fjfi.cvut.cz/en/cb-profile/stanema6>
- [13] Mandel, L., & Wolf, E. (2013). *Optical coherence and quantum optics*. Cambridge University Press.
- [14] Bazhenov, V. Yu., Soskin, M. S., & Vasnetsov, M. V. (1992). Screw Dislocations in Light Wavefronts. *Journal of Modern Optics*, 39(5), 985–990. <https://doi.org/10.1080/09500349214551011>
- [15] Andrews, G. E., Askey, R., & Roy, R. (1999). *Special functions* (No. 71). Cambridge University Press.
- [16] Beijersbergen, M. W., Coerwinkel, R. P. C., Kristensen, M., & Woerdman, J. P. (1994). Helical-wavefront laser beams produced with a spiral phaseplate. *Optics Communications*, 112(5-6), 321–327. [https://doi.org/10.1016/0030-4018\(94\)90638-6](https://doi.org/10.1016/0030-4018(94)90638-6)
- [17] Rotschild, C., Zommer, S., Moed, S., Hershcovitz, O., & Lipson, S. G. (2004). Adjustable spiral phase plate. *Applied Optics*, 43(12), 2397. <https://doi.org/10.1364/ao.43.002397>
- [18] Beijersbergen, M. W., Allen, L., van der Veen, H. E. L. O., & Woerdman, J. P. (1993). Astigmatic laser mode converters and transfer of orbital angular momentum. *Optics Communications*, 96(1-3), 123–132. [https://doi.org/10.1016/0030-4018\(93\)90535-d](https://doi.org/10.1016/0030-4018(93)90535-d)
- [19] Marrucci, L., Manzo, C., & Paparo, D. (2006). Optical Spin-to-Orbital Angular Momentum Conversion in Inhomogeneous Anisotropic Media. *Physical Review Letters*, 96(16). <https://doi.org/10.1103/physrevlett.96.163905>
- [20] Arlt, J., Dholakia, K., Allen, L., & Padgett, M. J. (1998). The production of multiringed Laguerre–Gaussian modes by computer-generated holograms. *Journal of Modern Optics*, 45(6), 1231–1237. <https://doi.org/10.1080/09500349808230913>
- [21] Bryngdahl, O. (1974). Optical map transformations. *Optics Communications*, 10(2), 164–168. [https://doi.org/10.1016/0030-4018\(74\)90046-7](https://doi.org/10.1016/0030-4018(74)90046-7)
- [22] Staněk, M. (2020). *Optical Transforms and Optical Angular Momentum Manipulation* [Unpublished research project]. ČVUT FJFI. Available from <http://physics.fjfi.cvut.cz/en/cb-profile/stanema6>
- [23] Schlederer, F., Krenn, M., Fickler, R., Malik, M., & Zeilinger, A. (2016). Cyclic transformation of orbital angular momentum modes. *New Journal of Physics*, 18(4), 043019. <https://doi.org/10.1088/1367-2630/18/4/043019>
- [24] Leach, J., Padgett, M. J., Barnett, S. M., Franke-Arnold, S., & Courtial, J. (2002). Measuring the Orbital Angular Momentum of a Single Photon. *Physical Review Letters*, 88(25). <https://doi.org/10.1103/physrevlett.88.257901>
- [25] Wei, H., Xue, X., Leach, J., Padgett, M. J., Barnett, S. M., Franke-Arnold, S., Yao, E., & Courtial, J. (2003). Simplified measurement of the orbital angular momentum of single photons. *Optics Communications*, 223(1-3), 117–122. [https://doi.org/10.1016/S0030-4018\(03\)01619-5](https://doi.org/10.1016/S0030-4018(03)01619-5)

- [26] Berkhout, G. C. G., Lavery, M. P. J., Courtial, J., Beijersbergen, M. W., & Padgett, M. J. (2010). Efficient Sorting of Orbital Angular Momentum States of Light. *Physical Review Letters*, *105*(15). <https://doi.org/10.1103/physrevlett.105.153601>
- [27] Isdrailă, T.-A., Kusko, C., & Ionicioiu, R. (2019). Cyclic permutations for qudits in d dimensions. *Scientific Reports*, *9*(1). <https://doi.org/10.1038/s41598-019-42708-7>
- [28] Gao, X., Krenn, M., Kysela, J., & Zeilinger, A. (2019). Arbitrary d -dimensional Pauli X gates of a flying qudit. *Physical Review A*, *99*(2). <https://doi.org/10.1103/physreva.99.023825>
- [29] Nielsen, M. A., & Chuang, I. L. (2000). *Quantum computation and quantum information*. Cambridge University Press.
- [30] Cirac, J. I., & Zoller, P. (1995). Quantum Computations with Cold Trapped Ions. *Physical Review Letters*, *74*(20), 4091–4094. <https://doi.org/10.1103/physrevlett.74.4091>
- [31] Gershenfeld, N. A., & Chuang, I. L. (1997). Bulk Spin-Resonance Quantum Computation. *Science*, *275*(5298), 350–356. <https://doi.org/10.1126/science.275.5298.350>
- [32] DiCarlo, L., Chow, J. M., Gambetta, J. M., Bishop, L. S., Johnson, B. R., Schuster, D. I., Majer, J., Blais, A., Frunzio, L., Girvin, S. M., & Schoelkopf, R. J. (2009). Demonstration of two-qubit algorithms with a superconducting quantum processor. *Nature*, *460*(7252), 240–244. <https://doi.org/10.1038/nature08121>
- [33] Kok, P., Munro, W. J., Nemoto, K., Ralph, T. C., Dowling, J. P., & Milburn, G. J. (2007). Linear optical quantum computing with photonic qubits. *Reviews of Modern Physics*, *79*(1), 135–174. <https://doi.org/10.1103/revmodphys.79.135>
- [34] Zeilinger, A. (1981). General properties of lossless beam splitters in interferometry. *American Journal of Physics*, *49*(9), 882–883. <https://doi.org/10.1119/1.12387>
- [35] Yurke, B., McCall, S. L., & Klauder, J. R. (1986). SU(2) and SU(1,1) interferometers. *Physical Review A*, *33*(6), 4033–4054. <https://doi.org/10.1103/physreva.33.4033>
- [36] Reck, M., Zeilinger, A., Bernstein, H. J., & Bertani, P. (1994). Experimental realization of any discrete unitary operator. *Physical Review Letters*, *73*(1), 58–61. <https://doi.org/10.1103/physrevlett.73.58>
- [37] Cerf, N. J., Adami, C., & Kwiat, P. G. (1998). Optical simulation of quantum logic. *Physical Review A*, *57*(3), R1477–R1480. <https://doi.org/10.1103/physreva.57.r1477>
- [38] Babazadeh, A., Erhard, M., Wang, F., Malik, M., Nouroozi, R., Krenn, M., & Zeilinger, A. (2017). High-Dimensional Single-Photon Quantum Gates: Concepts and Experiments. *Physical Review Letters*, *119*(18). <https://doi.org/10.1103/physrevlett.119.180510>
- [39] Davis, B. S., & Kaplan, L. (2013). Transverse phase variation of a Gaussian beam. *Journal of Optics*, *15*(7), 075706. <https://doi.org/10.1088/2040-8978/15/7/075706>
- [40] Goodman, J. W. (2005). *Introduction to Fourier Optics* (3rd ed.). Roberts.